algorithms

MDPI

Article

A Web-Based Analytical Framework for Infectious-Disease Forecasting and Chest X-Ray Image Analysis in Emergency Conditions

Maksym Saliutin [1], Yuriy Kondratenko [1], Ievgen Sidenko [1,*], Galyna Kondratenko [1] and Dmytro Chumachenko [2]

[1] Intellectual Information Systems Department, Petro Mohyla Black Sea National University, 68th Desantnykiv Str., 10, 54003 Mykolaiv, Ukraine; salyutin1@gmail.com (M.S.); yuriy.kondratenko@chmnu.edu.ua (Y.K.); halyna.kondratenko@chmnu.edu.ua (G.K.)

[2] Mathematical Modelling and Artificial Intelligence Department, National Aerospace University "Kharkiv Aviation Institute", Vadyma Manka Str., 17, 61001 Kharkiv, Ukraine; d.chumachenko@khai.edu

* Correspondence: ievgen.sidenko@chmnu.edu.ua; Tel.: +380-938837915

Abstract

The spread of infectious diseases under wartime and resource-constrained conditions creates a need for analytical tools that support both population-level epidemiological monitoring and preliminary patient-level image analysis. This study develops and evaluates a web-based analytical framework incorporating two complementary modules: infectious-disease forecasting and chest X-ray image analysis. For epidemiological forecasting, ARIMA, deep neural network (DNN), and long short-term memory (LSTM) models were evaluated to compare statistical, feed-forward neural-network, and recurrent neural-network approaches to one-month-ahead prediction using Ukrainian epidemiological data from 2020 to 2023. For chest X-ray analysis, YOLOv8 and YOLOv11 nano and small configurations were compared in a proof-of-concept experiment involving five pulmonary categories. The two analytical modules were integrated at the application level within a common web-based interface providing data upload, model selection, analysis, and result visualization. Under the adopted one-month-ahead hold-out evaluation, DNN and LSTM generally provided lower forecasting errors than the ARIMA baseline. In the image-analysis experiment, YOLOv11s produced the highest validation mAP@0.5:0.95 among the evaluated configurations, reaching 0.74. However, the public chest X-ray dataset had been augmented by its provider before acquisition, and the present image-analysis evaluation used training and validation partitions without an independent test subset for final performance assessment. Therefore, the reported image-analysis metrics characterize only the adopted validation partition, may overestimate performance on independent data, and should not be interpreted as estimates of clinical or external generalization. In addition, the manually prepared bounding-box annotations were not independently verified by a qualified clinical expert. Accordingly, the image-analysis component should be regarded as a proof-of-concept computational evaluation rather than a clinically validated diagnostic system. The developed prototype demonstrates the technical feasibility of providing epidemiological forecasting and preliminary chest X-ray image analysis within a common application environment for emergency and resource-constrained settings.

Keywords: infectious disease forecasting; YOLOv11; LSTM; ARIMA; chest X-ray image analysis; deep learning; object detection; web-based analytical framework

Check for updates

Academic Editors: Juvenal Rodriguez-Resendiz and Omneya A. Attallah

Received: 19 September 2026
Revised: 10 October 2026
Accepted: 15 October 2026
Published: 18 October 2026

Copyright: © 2026 by the authors. Licensee MDPI, Basel, Switzerland. This article is an open access article distributed under the terms and conditions of the Creative Commons Attribution (CC BY) license.

1. Introduction

Forecasting the prevalence of infectious diseases under wartime conditions represents a challenging task in time series analysis due to dynamic and uncertain environmental factors [1,2]. The military conflict in Ukraine has led to a serious deterioration in living conditions, which increases the risk of spreading infectious diseases. The destruction of medical infrastructure and lack of proper access to medical services in many regions weaken the ability to control the disease [3–5]. The displacement of the population due to the hostilities creates conditions for mass contacts in shelters and temporary accommodation centers, where there is a lack of proper sanitary and hygienic standards, which contributes to the transmission of infectious diseases. In particular, the war increases the vulnerability of the population to infectious diseases due to deteriorating immunity, stress factors, and lack of access to necessary medicines, among other things [6]. Official surveillance of infectious diseases in Ukraine was disrupted by Russia's invasion in 2022, which led to problems with tracking and containing epidemics. Looking at open-source data from EPIWATCH, one can see the numbers for the most commonly reported cases of diseases, with figures from official sources [7]. There was an increase in the total number of reports of infectious diseases compared to the period before the invasion (Figure 1).

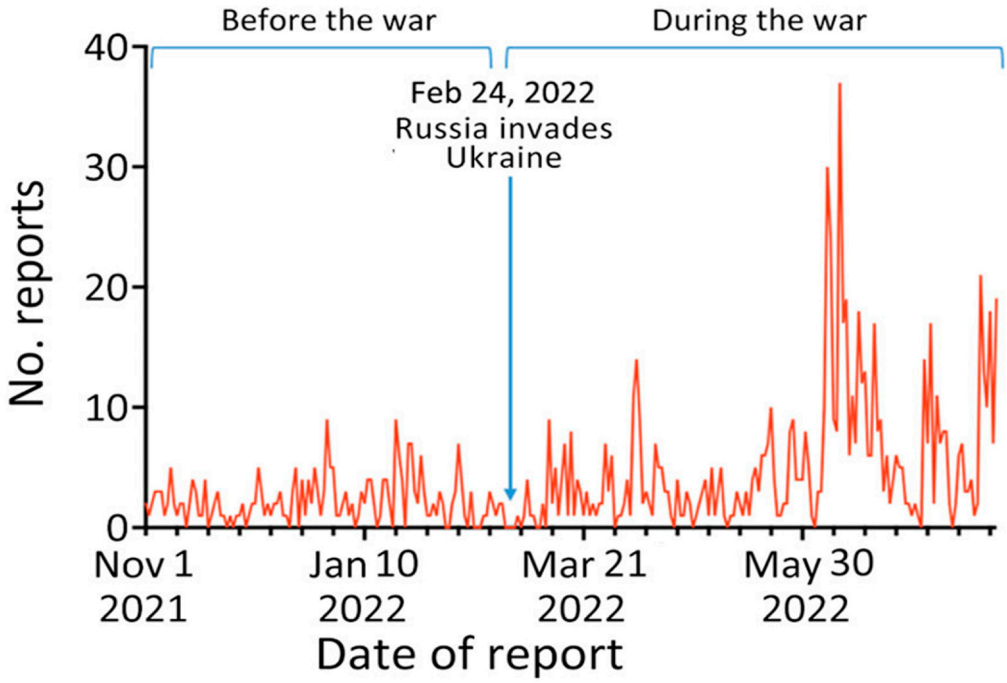


Figure 1. EPIWATCH daily reports on outbreaks in Ukraine before and during the Russian invasion, 1 November 2021–31 July 2022 [7,8].

Looking at the behavior of infectious diseases, we can take into account the large-scale measles epidemic that affected Ukraine in 2019, partly due to low vaccination coverage. Although reported cases have decreased significantly, the recent shortage of vaccines against many diseases poses a threat to society [8,9]. Despite the availability of machine learning approaches for either epidemiological forecasting or medical image analysis, most existing solutions address these tasks independently, without integrating them into a unified framework. In application-oriented scenarios, especially under emergency conditions, there is a need for systems that can provide both disease-spread forecasting and preliminary image-analysis functionality within a common analytical environment. The main contributions of this study are as follows:

- Development of an application-level analytical framework that brings together two complementary tasks: population-level infectious disease forecasting and individual-level chest X-ray image analysis within a unified system.
- Comparative evaluation of ARIMA, DNN, and LSTM approaches for one-month-ahead infectious disease forecasting using Ukrainian epidemiological data collected for 2020–2023. The experiments consider measles, acute respiratory infections, and influenza, allowing statistical and neural-network forecasting approaches to be assessed under the same application scenario.
- Comparative proof-of-concept evaluation of YOLOv8 and YOLOv11 object-detection architectures for chest X-ray image analysis. Nano and small configurations of both model generations are evaluated for five annotated categories—bacterial pneumonia, COVID-19, tuberculosis, viral pneumonia, and normal lungs—under the same validation-partition protocol.
- Implementation of a web-based prototype that provides access to both analytical modules through a common interface. The developed system supports epidemiological data upload, forecasting-model selection and visualization of predictions, as well as chest X-ray upload and visualization of image-analysis results.

Unlike approaches that address epidemiological forecasting and medical image analysis as separate application scenarios, the proposed prototype provides access to both functionalities within a common web-based environment. The current implementation integrates these components at the application level and is presented as a proof-of-concept analytical prototype for resource-constrained and emergency-condition scenarios.

2. Comparative Analysis of Existing Approaches and Research Gap

Research related to the proposed system can be divided into two principal directions: epidemiological time series forecasting and automated analysis of thoracic medical images. Although both directions contribute to infectious disease management, they are usually investigated independently. Forecasting methods operate at the population level and estimate future incidence dynamics, whereas image-based methods operate at the individual-image level and provide computational analysis of radiological data. Under wartime and resource-constrained conditions, these tasks can be considered complementary within a unified analytical framework.

The numerical results reported in the reviewed studies cannot be compared directly because the corresponding experiments differ in terms of diseases, geographical regions, forecasting horizons, imaging modalities, dataset composition, model configurations, and evaluation metrics. Therefore, the following analysis focuses on the methodological scope, functional coverage, application context, and limitations of the considered approaches rather than on a direct ranking of their reported numerical results.

Classical statistical models remain relevant as interpretable baselines for infectious-disease forecasting. In [10], the ARIMA model was applied to COVID-19 morbidity and mortality data from India. The obtained forecasts were consistent with the observed dynamics, demonstrating that autoregressive models can capture short-term temporal patterns when sufficiently regular historical observations are available. However, the use of a single statistical model limits the ability to represent nonlinear dependencies and abrupt structural changes that may arise during emergencies, population displacement, or disruptions in disease surveillance.

A direct comparison between statistical and neural network forecasting was performed in [11], where ARIMA and LSTM models were used to predict daily COVID-19 cases and mortality in two regions of Indonesia. The LSTM model demonstrated better forecasting performance according to RMSE and MAPE. This result indicates that recurrent neural

networks can provide advantages when the time series contains nonlinear and long-term temporal dependencies. Nevertheless, the experiment considered a short 13-day forecasting horizon and a single infectious disease, while no medical-image-analysis functionality was included.

The study in [12] further developed the idea of combining statistical and deep-learning methods. Hybrid PSO-LSTM-ARIMA, MLR-LSTM-ARIMA, and BPNN-LSTM-ARIMA models were evaluated using epidemiological data from Germany and Japan. The BPNN-LSTM-ARIMA configuration achieved the best results according to MSE, RMSE, and MAE. Hybridization can increase predictive capacity by combining linear and nonlinear representations; however, it also increases model complexity and the number of parameters that must be configured. Moreover, the proposed approach remains limited to epidemiological forecasting and does not include a patient-level medical-image-analysis component.

The model presented in [13] combines an improved susceptible-infected formulation with NLP and LSTM components to account for differences in infection rates between individuals. Its main contribution is the incorporation of additional contextual information into short-term forecasting. The model reduced the average prediction error for several countries compared with alternative approaches. At the same time, the study remained focused on short-term COVID-19 forecasting and did not address radiological image analysis or integration within a combined analytical software environment.

Taken together, studies [10–13] demonstrate a transition from classical ARIMA-based forecasting to recurrent and hybrid neural network models. Their results support the comparative evaluation of statistical and deep learning approaches. However, the reviewed forecasting studies are primarily focused on COVID-19, are evaluated outside wartime conditions, and do not integrate population-level forecasts with individual image-based analysis.

The second group of studies focuses on computer-aided analysis of thoracic images. In [14], the Lung-DT framework combines YOLOv8 with digital twin and IoT technologies for chest X-ray analysis. Importantly, one of the public datasets used in that study was the same "Lungs Disease Dataset (4 Types)" employed in the present work. However, Lung-DT combined this dataset with an additional public chest X-ray dataset, forming a substantially larger unified dataset, and applied a different training and evaluation protocol. The authors reported validation and test accuracies of 96.6% and 96.8%, respectively. These values cannot be directly compared with the results of the present study because the dataset composition, data partitioning, task formulation, annotation protocol, and evaluation metrics differ. In particular, the present study evaluates bounding-box-based YOLO detection using mAP@0.5:0.95, whereas Lung-DT primarily reports classification-oriented accuracy, precision, recall, and F1-score. Nevertheless, the results of [14] confirm the applicability of the selected public chest X-ray data to automated pulmonary image analysis and provide a relevant reference point for the present experiments.

The influence of architecture selection and training configuration on respiratory disease classification was investigated in [15]. Pre-trained convolutional networks, including ResNet50, DenseNet121, EfficientNetB4, and MobileNetV2, were evaluated using chest X-ray images. The study showed that performance depends not only on the architecture but also on the learning rate, optimizer, dropout, and other hyperparameters. This finding supports the need for comparative model evaluation under a consistent experimental protocol. However, the study addresses image classification only and does not include disease incidence forecasting, object localization, or an integrated user-oriented platform.

The authors of [16] proposed an improved YOLOv8 model for detecting lung-cancer targets and classifying their subtypes in CT images. High-resolution attention, multi-scale feature interaction, modified spatial-pyramid pooling, and an alternative IoU-based loss function were introduced to improve the recognition of small targets. The study illustrates

the use of architecture-level modifications for a specialized medical-image task. Its experimental scope is limited to lung cancer and CT imaging, whereas no epidemiological component or comparison with newer YOLO generations is provided.

A YOLOv8-based method for detecting COVID-19, H1N1 influenza, and cancer in CT scans was evaluated in [17]. The study reported an average processing time of 2.38 s for its YOLO-based image-analysis procedure. Consequently, it does not establish whether newer YOLO architectures provide a more favorable balance between accuracy, model complexity, and inference speed.

The comparative study in [18] evaluates YOLOv8, YOLOv9, YOLOv10, YOLOv11, and Faster R-CNN for weed detection. Although the application domain is not medical, the study provides relevant cross-domain evidence concerning the speed-accuracy trade-off of recent object-detection architectures. In particular, its results demonstrate that the newest model version is not necessarily the most accurate in every task and that architecture selection should be based on experimental comparison rather than model recency alone. The direct transferability of these results to chest X-ray analysis is limited because agricultural and medical images differ substantially in visual structure, object scale, annotation characteristics, and acceptable error levels.

The image-based studies therefore confirm the applicability of convolutional and YOLO-based architectures to pulmonary image analysis. At the same time, most of them either evaluate a single detector family, focus on a single disease or imaging modality, or remain disconnected from epidemiological forecasting. The comparison criteria in Table 1 were selected to reflect the principal functional requirements of the proposed system and to identify the corresponding research gap. The "Epidemiological forecasting" criterion indicates whether a study supports population-level prediction of disease incidence, whereas "Thoracic image analysis" reflects the availability of patient-level analysis of chest imaging data. The "Integrated operational framework" criterion was included to distinguish standalone algorithmic studies from solutions that combine analytical functionality within an application-oriented system. Finally, the "Principal limitation relative to the proposed task" criterion summarizes the main methodological or functional restriction of each study with respect to the combined forecasting and image-analysis scenario considered in this work. The functional coverage of the reviewed studies is summarized in Table 1.

The comparison reveals four principal research gaps. First, the reviewed forecasting studies [10–13] do not include an image-analysis component, while the medical-image studies [14–17] do not estimate future disease incidence. As a result, population-level epidemiological forecasting and individual-level image analysis remain separated into different analytical workflows.

Second, several studies rely on a single statistical model or detector architecture. Although studies [11,12,15,18] demonstrate the value of comparative evaluation, there remains a need to compare classical forecasting, feed-forward neural network, recurrent neural network, and modern object-detection approaches under consistent data-preparation and evaluation conditions.

Third, most epidemiological studies focus on COVID-19 in non-wartime settings. They do not explicitly consider the combined effects of disrupted surveillance, population displacement, restricted access to healthcare facilities, and limited diagnostic resources. These factors are particularly relevant to infectious disease monitoring in Ukraine.

Fourth, many existing works evaluate algorithms as independent experimental models without integrating them into an accessible system. An application-level analytical environment can instead provide common access to epidemiological and radiological data processing, model selection, analysis initiation, and result visualization through a unified interface.

Table 1. Summary of related studies and their functional coverage.

Ref.	Epidemiological Forecasting	Thoracic Image Analysis	Integrated Operational Framework	Principal Limitation Relative to the Proposed Task
[10]	Yes	No	No	A single statistical model and a single disease; nonlinear and emergency-driven changes are not explicitly addressed.
[11]	Yes	No	No	Short forecasting horizon; no image-analysis component.
[12]	Yes	No	No	Forecasting-only solution with increased hybrid-model complexity.
[13]	Yes	No	No	Short-term COVID-19 prediction without radiological analysis.
[14]	No	Yes	Yes	Patient-level image analysis without epidemiological forecasting or comparison of YOLO generations.
[15]	No	Yes	No	Image classification and hyperparameter analysis only.
[16]	No	Yes	No	Specialized for one pathology and one imaging modality.
[17]	No	Yes	No	No comparison with newer YOLO architectures and no forecasting module.
[18]	No	Non-medical	No	Provides cross-domain architecture comparison but has limited direct medical applicability.
This study	Yes	Yes	Yes	Combines population-level forecasting and preliminary image-based analysis in a web system intended for resource-constrained wartime conditions.

Accordingly, the research problem addressed in this study is the development and experimental evaluation of an application-level analytical framework that provides complementary population-level infectious-disease forecasting and individual-level chest X-ray image analysis within a common software environment. The forecasting subsystem compares ARIMA, DNN, and LSTM models using Ukrainian incidence data for measles, acute respiratory infections, and influenza. The image analysis subsystem compares the nano and small configurations of YOLOv8 and YOLOv11 for five chest X-ray categories: bacterial pneumonia, COVID-19, tuberculosis, viral pneumonia, and normal lungs. Both subsystems are incorporated into a web-based interface intended to support analytical work under resource-constrained and wartime conditions.

The proposed framework differs from the reviewed approaches not by introducing a single universally superior algorithm, but by combining complementary analytical tasks and enabling model comparison within a common application environment. The resulting system is presented as a proof-of-concept application-level framework for epidemiological

forecasting and preliminary computer-aided image analysis and should not be interpreted as a clinically validated diagnostic system or as a replacement for medical expertise.

3. Materials and Methods

Machine learning approaches have been increasingly applied to epidemiological modeling and infectious disease analysis [19–22], as well as to intelligent control [23], image recognition [24], and medical image processing [25]. At the same time, recent studies emphasize that the effectiveness of a particular model depends strongly on the structure of the input data, the application scenario, and the selected training and evaluation protocol [26]. Therefore, rather than relying on a single modeling paradigm, this study evaluates several complementary approaches for the two analytical tasks considered.

Recent time series studies demonstrate the diversity of forecasting formulations and application scenarios, including discrete count-data models [27], transformer-based forecasting in healthcare [28], disease incidence forecasting combined with an interactive software environment [29], and time series modeling of measles outbreaks [30]. These examples indicate that forecasting-model selection should account for both the structure of the available data and the intended application scenario.

Related methodological studies have considered autoregressive modeling under spatial error structures [31] and scalable variable selection for spatial autoregressive models [32]. Machine learning approaches have also been applied to classification problems involving medical data [33]. These studies further illustrate the dependence of model design on data characteristics and task formulation.

For epidemiological forecasting, three approaches were selected: seasonal ARIMA, a feed-forward DNN, and an LSTM network. This selection enables comparison between a classical statistical model, a nonlinear feed-forward neural model, and a recurrent architecture designed to represent temporal dependencies. All three approaches were applied to monthly incidence data for measles, acute respiratory infections, and influenza collected in Ukraine for 2020–2023.

ARIMA-based approaches remain widely used for infectious disease and nonstationary time series forecasting [34–37]. Hybrid ARIMA-neural and related autoregressive approaches have also been investigated in other forecasting domains, including traffic-accident loss prediction and air-quality forecasting [38,39]. ARIMA has additionally been applied to interrupted time-series analysis of communicable-disease incidence [40].

Seasonal and hybrid SARIMA formulations have been evaluated across a range of forecasting tasks, including rainfall [41], monthly humidity [42], satellite-derived environmental time series [43], hospital admissions [44], economic indicators [45], atmospheric CO_2 concentrations [46], and infectious disease incidence [47]. Collectively, these studies demonstrate the applicability of seasonal autoregressive modeling to time series with different domains and temporal structures.

For chest X-ray analysis, YOLOv8 and YOLOv11 were selected as representative one-stage object-detection architectures. Nano and small configurations of both generations were evaluated to examine the influence of both detector generation and model capacity on the considered five category image analysis task. The overall methodology therefore consists of two independent processing pipelines. In the forecasting pipeline, historical monthly incidence observations are processed by the selected ARIMA, DNN, or LSTM model to generate a one-month-ahead disease incidence forecast. In the image-analysis pipeline, a chest X-ray image is processed by a trained YOLO detector to obtain the predicted pulmonary category, bounding-box localization, and confidence score. The outputs of both pipelines are subsequently made available through the common web-based application.

Because the epidemiological series considered in this study exhibited seasonal behavior, a seasonal ARIMA formulation was used as the statistical baseline. Autocorrelation and partial autocorrelation functions were examined to assess the temporal structure of each series; however, the cutoff points did not provide an unambiguous basis for manual order selection. Candidate configurations were therefore identified using the auto.arima procedure in R and compared using the Akaike information criterion (AIC) and root mean squared error (RMSE). For each disease, the selected configuration was fitted to the available historical observations and used to generate a one-month-ahead incidence forecast. Thus, the input of the statistical branch is the chronological morbidity series, whereas its output is the predicted incidence value for the subsequent monthly observation.

Other recent studies further illustrate the diversity of modern time series forecasting strategies, including transformer-based prediction of electric-vehicle charging demand [48], comparative ARIMA/SARIMA modeling of traffic loads [49], and Box–Cox-integrated SARIMA forecasting [50].

Deep neural architectures have likewise been applied to a variety of sequential-data problems, including DNN-based time series distribution estimation [51], hybrid LSTM-DNN modeling [52], DNN-based time series preprocessing and classification [53], and hybrid sequence-oriented signal modeling [54]. The broader adaptability of DNN-based architectures has also been demonstrated in cybersecurity [55], industrial information and control systems [56], edge computing applications [57], neural model protection [58], intelligent transportation systems [59], and image-based disease-related classification tasks [60].

For infectious disease forecasting, a feed-forward DNN model was implemented using the Keras Sequential API and Dense layers. The network included hidden layers with 128, 128, and 64 neurons using ReLU activation, followed by a single-neuron output layer for forecasting. Model training was monitored using the mean squared error (MSE) loss. The loss values were used exclusively to assess the convergence of the optimization process and should not be interpreted as classification or forecasting accuracy. The predictive performance of the forecasting models was evaluated separately using held-out epidemiological observations, as described in Section 4. The prepared historical incidence observations were supplied to the DNN input, and the single-neuron output layer returned the forecasted incidence value for the following month. In this way, the DNN provides a nonlinear feed-forward alternative to the seasonal ARIMA forecasting branch while producing the same type of final output.

LSTM networks are recurrent neural architectures designed to model temporal dependencies through gated memory mechanisms [61–71]. Their ability to preserve relevant information over extended sequences makes them suitable for non-stationary epidemiological time series, where current incidence may depend on observations from previous periods. In this study, LSTM was therefore evaluated as a nonlinear recurrent alternative to both the statistical ARIMA model and the feed-forward DNN approach. In this study, the LSTM model was used for one-step-ahead forecasting of infectious disease incidence based on historical observations. The input time series was transformed into sequential samples representing previous observations and their corresponding target values. These sequences were provided to the LSTM network, followed by a fully connected output layer producing the forecasted incidence value. Model parameters were optimized during training using the mean squared error loss, and the trained network was subsequently used to generate the one-month-ahead forecasts evaluated in Section 4. The main computational steps are summarized in Algorithm 1.

Algorithm 1. LSTM-based infectious-disease forecasting procedure

Input: historical incidence time series X
Output: one-step-ahead forecast $\hat{y}$

1. Load the historical epidemiological time series.
2. Prepare sequential input–target pairs from previous observations.
3. Reshape the input data into the format required by the LSTM network.
4. Initialize the LSTM forecasting model.
5. Add an LSTM layer for extracting temporal dependencies.
6. Add a fully connected output layer producing the forecast value.
7. Configure the model using mean squared error as the loss function.
8. Train the model on the prepared historical sequences.
9. Provide the most recent observation sequence to the trained model.
10. Generate the one-step-ahead disease-incidence forecast, $\hat{y}$.
11. Return $\hat{y}$.

The epidemiological dataset was obtained from the official website of the Center for Public Health of the Ministry of Health of Ukraine [72] and covers the period from 2020 to 2023. The source reports infectious disease morbidity according to reporting form No. 1 and includes both absolute numbers of registered cases and incidence indicators per 100,000 population. For the experiments conducted in this study, data on measles, acute respiratory infections (ARIs), and influenza were selected. The corresponding monthly observations were consolidated into unified chronological time series and subsequently used as input to the ARIMA, DNN, and LSTM forecasting models. Each model produced a one-month-ahead incidence forecast for the selected disease.

A common one-month-ahead evaluation protocol was applied to the forecasting models. December 2023 was excluded from the data used for model fitting and retained as a held-out observation. This evaluation represents a single-origin one-step-ahead hold-out experiment and was designed to provide a common preliminary comparison of the three forecasting approaches under the same temporal setting. It does not constitute a rolling-origin or repeated out-of-sample validation across multiple forecasting origins.

ARIMA, DNN, and LSTM were then used to forecast the incidence value for this month separately for each considered disease, and the predicted values were compared with the corresponding observed data. This procedure provided a common evaluation scenario for the three forecasting approaches.

YOLO-based one-stage detectors were selected because of their favorable balance between detection performance and computational efficiency [73,74]. Recent studies have also considered YOLOv11-based processing in medical image region-of-interest applications [75], while optimized YOLOv8 architectures have been investigated for multi-scale object detection [76]. These developments provide additional motivation for comparing YOLOv8 and YOLOv11 under the same task-specific experimental protocol rather than selecting a detector solely on the basis of model generation.

During model training, three principal optimization losses were monitored: box loss for bounding-box localization, classification loss for class prediction, and Distribution Focal Loss (DFL) for bounding-box coordinate estimation. The resulting validation-partition predictions were subsequently summarized using precision, recall, and mean average precision, with mAP@0.5:0.95 used as the principal metric for the internal comparison of the evaluated detector configurations.

All four configurations were trained using the same image resolution and dataset-preparation procedure and were compared under the same validation-partition protocol.

The nano configurations were trained for 50 epochs, whereas the small configurations were trained for 10 epochs. The obtained results were subsequently compared using the detection metrics described in Section 4.

The lung disease dataset was taken from the official Kaggle website [77]. The dataset contains chest X-rays. The dataset was assembled by the dataset provider from several source datasets, with duplicate images removed using VisiPics. It contains four disease categories (bacterial pneumonia, COVID-19, tuberculosis, and viral pneumonia) and a normal-lung category. The dataset provider subsequently expanded the dataset approximately sixfold through data augmentation, resulting in approximately 10,000 images.

It should be noted that the augmentation procedure had been applied by the dataset provider before the dataset was obtained for the present study. The available dataset did not provide explicit provenance links between each augmented image and its corresponding original source image. Consequently, the subsequent random train-validation partition could not be performed at the level of original-image groups.

The public dataset provides image-level category information through its predefined disease folders but does not contain the bounding-box annotations required for YOLO-based object detection. Therefore, bounding-box annotations were manually prepared for the images using Label Studio, while the corresponding category labels were retained from the source dataset. The annotation procedure was performed for the purpose of constructing an object-detection dataset for the present computational experiment. The manually prepared bounding-box annotations were not independently reviewed or validated by a qualified radiologist or other clinical specialist. Therefore, these annotations should be regarded as technical annotations used for the machine-learning experiment rather than as independently verified clinical ground truth.

An example of the bounding-box annotation procedure applied to the chest X-ray images is shown in Figure 2.

The dataset partition used in the present experiments contained 6054 training images and 2016 validation images. The class distribution in the training subset was as follows: 1205 bacterial pneumonia images, 1218 COVID-19 images, 1207 normal-lung images, 1220 tuberculosis images, and 1204 viral pneumonia images. The validation subset contained 401 bacterial pneumonia images, 406 COVID-19 images, 402 normal-lung images, 406 tuberculosis images, and 401 viral pneumonia images.

The present experimental protocol used the available training and validation partitions for model development and validation-partition assessment. No separately defined independent test subset was used for final performance assessment. Because the public dataset had been augmented before acquisition and the provenance of the augmented images was unavailable, source-level grouping could not be reconstructed.

Therefore, although no image file was intentionally assigned to both subsets, the possibility that transformed variants originating from the same source image occurred in different subsets cannot be completely excluded. To provide an additional descriptive assessment of potential cross-partition similarity, a near-duplicate analysis was performed between all 6054 training and 2016 validation images. Exact byte-level duplicates were first assessed using SHA-256 hashes. Perceptual similarity was then evaluated using 64-bit perceptual hashes (pHash) computed with the ImageHash library (phash, hash_size = 8) after EXIF orientation correction and RGB conversion. Each validation image was compared exhaustively with every training image using the Hamming distance between perceptual hashes, resulting in 12,204,864 cross-partition comparisons. Thresholds of 0, $\leq$2, $\leq$4, $\leq$6, $\leq$8, and $\leq$10 were examined as a sensitivity analysis, with a Hamming distance of $\leq$4 used as a strict descriptive near-duplicate candidate threshold. The analysis

was not intended to reconstruct unavailable source-image provenance or to establish source-level independence.

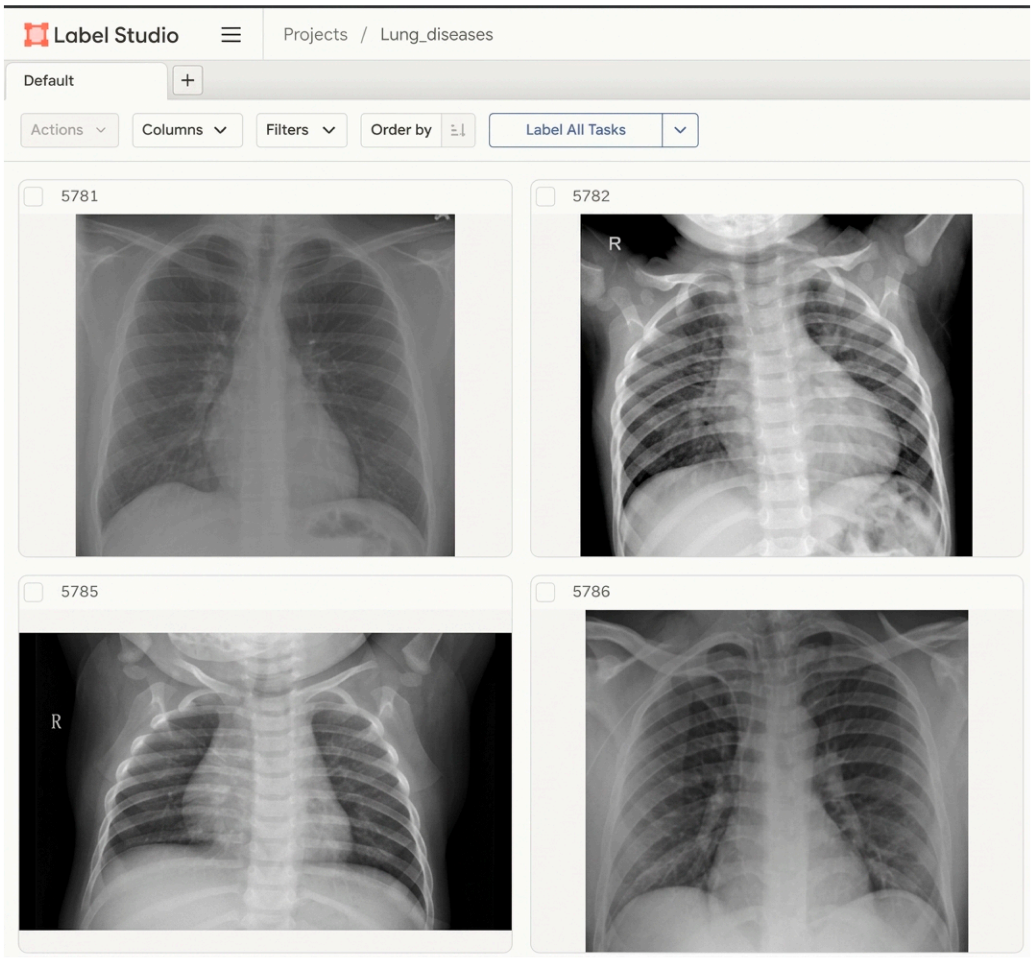


Figure 2. Example of the bounding-box annotation procedure used to prepare the chest X-ray dataset in Label Studio.

During YOLO training, each chest X-ray image was processed together with its corresponding manually prepared bounding-box annotation and class label. The models were optimized to jointly determine the spatial localization of the annotated region and its associated pulmonary category. During inference, the trained detector receives a chest X-ray image without ground-truth annotations and returns the detected bounding box, predicted class, and corresponding confidence score. These outputs form the result of the image-analysis pipeline and are subsequently visualized in the web-based application.

The forecasting and image-analysis pipelines operate independently at the model level. Their integration is implemented at the application level through a common web interface: epidemiological observations are processed by the forecasting subsystem, whereas chest X-ray images are processed by the selected YOLO model. No intermediate representations or predictions are exchanged between the two models.

4. Results

This section reports the experimental results of the forecasting and image-analysis models under the data partitions and hold-out procedures defined in Section 3. The forecasting results characterize the adopted one-month-ahead hold-out scenario. For the image-analysis component, all reported metrics were obtained on the validation partition of a public dataset that had been augmented by the provider before acquisition. Because

the provenance of the augmented images was unavailable, transformed variants derived from the same source image may occur in both the training and validation subsets. No independent test subset was used, and the manually prepared bounding-box annotations were not independently verified by a qualified clinical expert. Consequently, the image-analysis metrics reported in this section may be optimistic and should be interpreted only as validation-partition results rather than as estimates of performance on independent or clinical data. The descriptive cross-partition similarity audit identified no byte-identical TRAIN–VALIDATION image pairs according to SHA-256 hashing. Using the strict pHash Hamming-distance threshold of ≤ 4, 54 candidate cross-partition pairs were identified, involving 47 training images (0.78% of the training subset) and 41 validation images (2.03% of the validation subset). Among these 54 candidate pairs, the median Hamming distance was 4. Across all validation images, the median distance to the nearest training image was 10. The strict-threshold similarity graph contained 34 cross-partition connected components, with a maximum component size of eight images. These candidate matches represent visual similarity only and do not establish that the corresponding images originated from the same source image.

The training and validation loss curves and the corresponding precision, recall, and mAP metrics for the four evaluated YOLO configurations are presented in Figures 3–6.

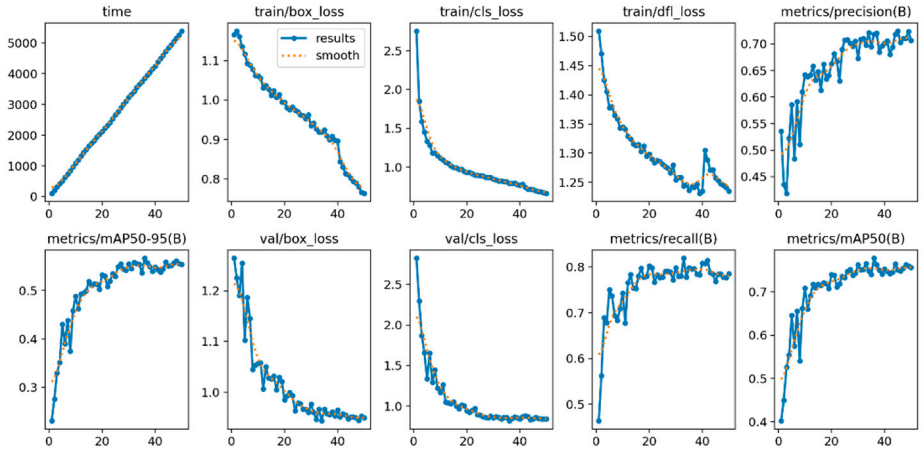


Figure 3. Training and validation losses and detection metrics obtained during training of the YOLOv8n model.

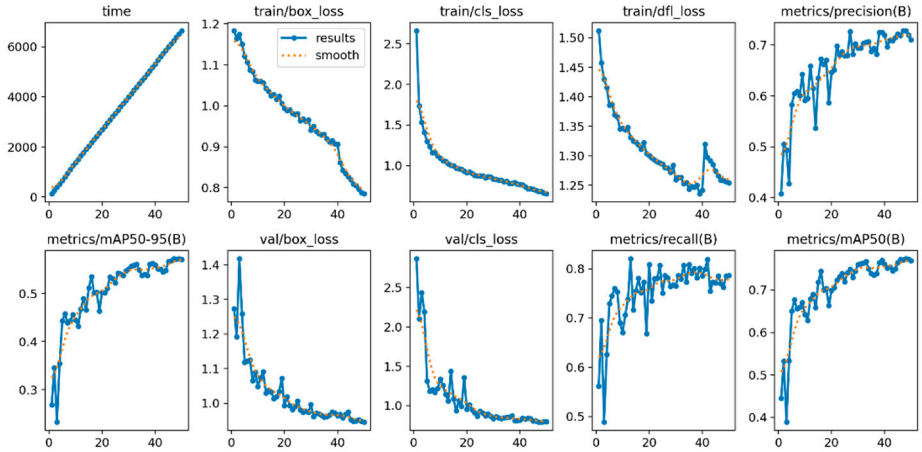


Figure 4. Training and validation losses and detection metrics obtained during training of the YOLOv8s model.

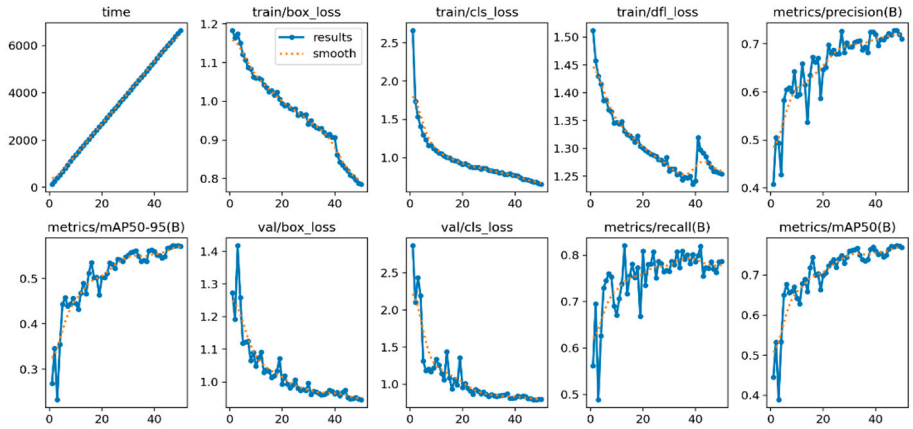


Figure 5. Training and validation losses and detection metrics obtained during training of the YOLOv11n model.

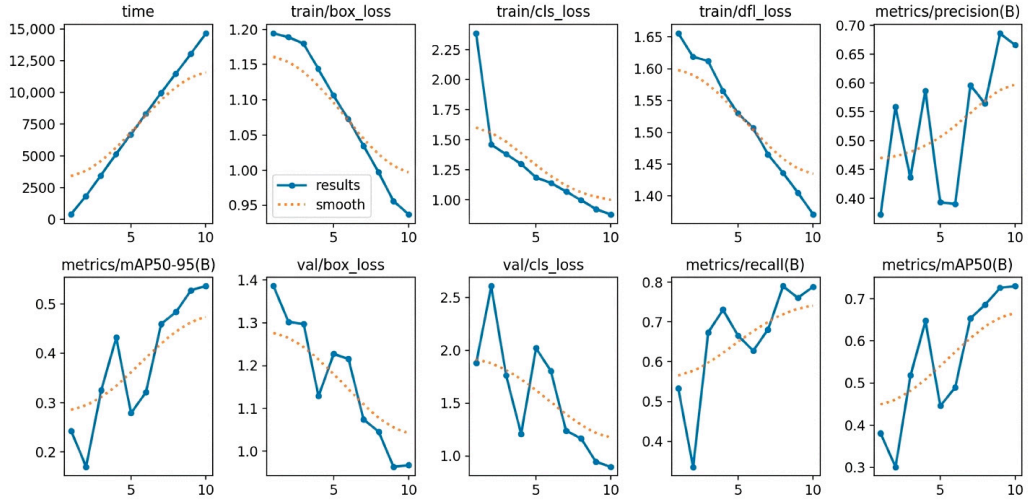


Figure 6. Training and validation losses and detection metrics obtained during training of the YOLOv11s model.

The loss curves in Figures 3–6 provide additional information on the optimization behavior of the evaluated YOLO configurations. For YOLOv8n, YOLOv8s, and YOLOv11n, the training box, classification, and distribution focal losses generally decrease as training progresses. The corresponding validation losses exhibit the same overall downward tendency, although short-term fluctuations are present. At the same time, precision, recall, and mAP increase during training, indicating that the reduction in optimization losses is accompanied by higher metric values on the adopted validation partition.

The YOLOv11s curves exhibit greater epoch-to-epoch variability than those of the nano configurations. This behavior should be interpreted in the context of the shorter training schedule used for the small model, which comprised only 10 epochs compared with 50 epochs for the nano models. Despite these fluctuations, the principal loss components decrease over the training interval, while the detection metrics generally improve. The presented curves therefore indicate model convergence within the applied training schedules; however, the fluctuations in the validation curves do not justify a categorical conclusion regarding the complete absence of overfitting. For this reason, the evaluated configurations are compared descriptively using their validation-partition metrics, particularly mAP@0.5:0.95, rather than training-loss values alone.

The precision-confidence curves for YOLOv8n and YOLOv8s (Figure 7) and for YOLOv11n and YOLOv11s (Figure 8) show how class-wise precision changes with the

confidence threshold. In general, stricter confidence thresholds retain fewer but more precise predictions, although class-specific fluctuations remain.

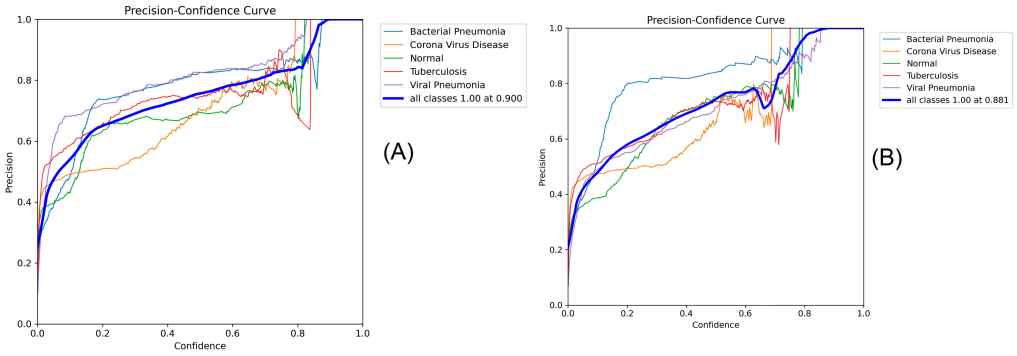


Figure 7. Precision and confidence curve for (**A**) YOLOv8n and (**B**) YOLOv8s.

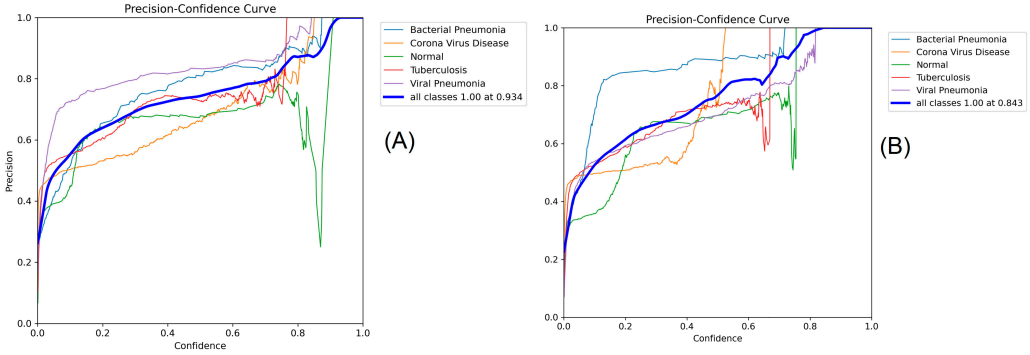


Figure 8. Precision and confidence curve for (**A**) YOLOv11n and (**B**) YOLOv11s.

In Figure 7A, representing YOLOv8n, the combined precision approached 1.0 at a confidence threshold of 0.900. For YOLOv8s, precision likewise increased at higher confidence thresholds. In Figure 8A, YOLOv11n reached a precision of 1.0 at a confidence threshold of 0.934, while YOLOv11s reached the same precision value at a lower threshold of 0.843. These curves describe the behavior of the evaluated models on the adopted validation partition at different confidence thresholds and should not be interpreted as evidence of diagnostic reliability or generalization to independent data.

The normal-lung and tuberculosis categories exhibit more pronounced precision fluctuations at high confidence thresholds than several other categories, indicating greater variability in the corresponding validation-partition predictions.

Representative model outputs obtained for images from the validation subset are presented in Figures 9–12. These examples are provided for qualitative illustration of the predictions produced by the evaluated YOLO configurations.

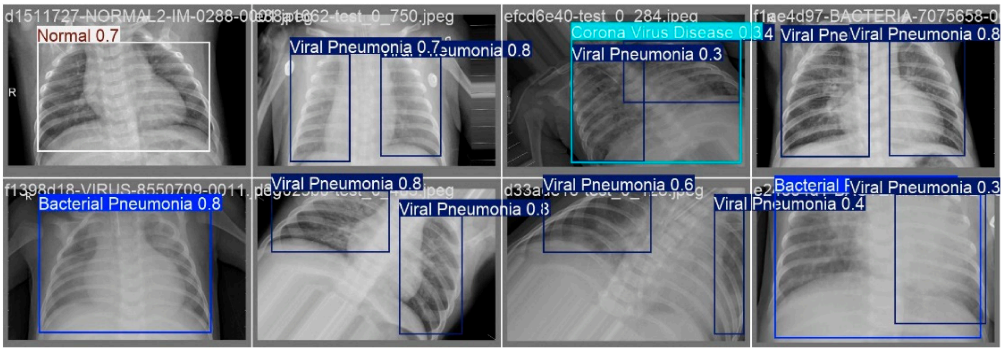


Figure 9. Representative validation-subset outputs produced by the YOLOv8n model.

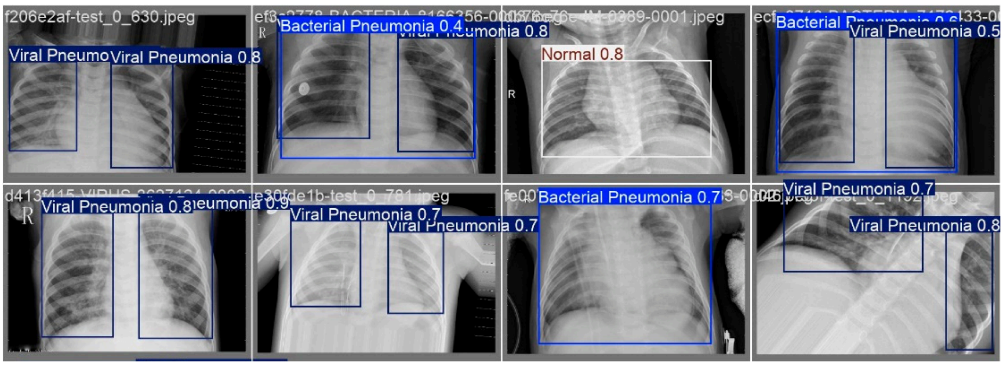


Figure 10. Representative validation-subset outputs produced by the YOLOv8s model.

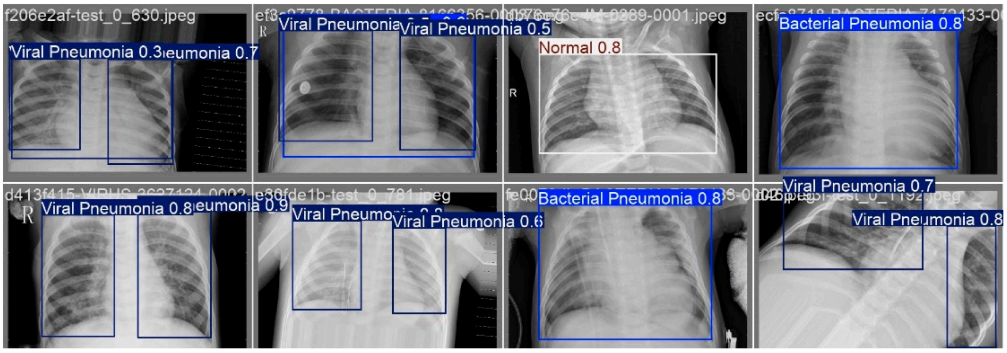


Figure 11. Representative validation-subset outputs produced by the YOLOv11n model.

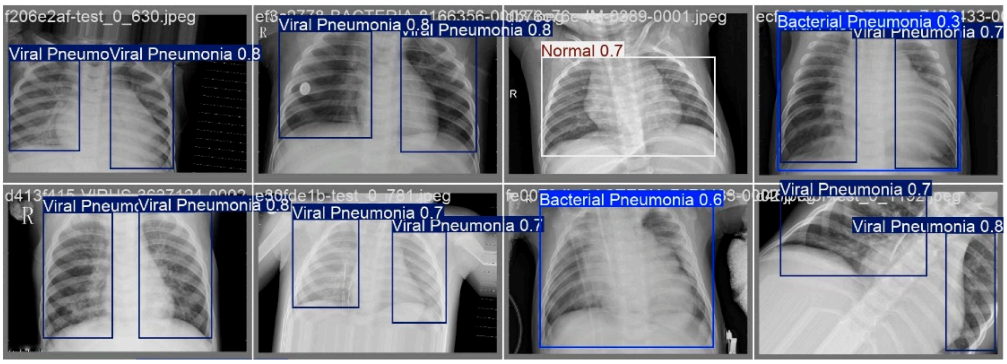


Figure 12. Representative validation-subset outputs produced by the YOLOv11s model.

Qualitative inspection of the validation examples shows that some images produce multiple class predictions with different confidence scores. These cases illustrate variability among predictions for visually similar annotated categories; however, they are presented only for qualitative illustration and are not used as quantitative evidence of model generalization. Some errors involve the normal-lung category and disease categories with visually subtle image patterns. These observations are limited to the current validation partition and do not support conclusions about clinical diagnostic behavior.

Among the evaluated configurations, YOLOv11s produced the highest validation mAP@0.5:0.95, reaching 0.74. This value characterizes only the adopted validation partition and should not be interpreted as an estimate of performance on independent datasets. Because the source dataset had been pre-augmented and the original-image provenance was unavailable, the possibility of cross-partition similarity or overlap cannot be excluded. Accordingly, the observed difference between YOLOv11s and the other configurations is interpreted only as a relative result within the present proof-of-concept evaluation.

The remaining configurations achieved lower mAP@0.5:0.95 values than YOLOv11s, as summarized in Table 2. These differences indicate variation in validation-partition metric values across model capacities and generations under the adopted protocol. Because no independent external test dataset or clinical validation was used, these results should not be interpreted in terms of diagnostic suitability.

Table 2. Validation-partition mAP@0.5:0.95 and final training statistics of the evaluated YOLO configurations.

YOLO Model	Training Time (min)	Validation mAP@0.5:0.95	Final Train Box Loss	Final Train Cls Loss	Final Train DFL Loss
YOLOv8n	89.83	0.702	0.7631	0.6576	1.235
YOLOv8s	191.31	0.713	0.9221	0.9334	1.352
YOLOv11n	110.6	0.724	0.7848	0.6496	1.254
YOLOv11s	242.86	0.74	0.9369	0.8775	1.371

It should also be noted that the absolute training-loss values should not be used as direct performance scores for ranking different model configurations. The final model comparison is therefore based primarily on detection metrics obtained for the validation subset, particularly mAP@0.5:0.95.

The four YOLO configurations produced different validation-partition metric values, with YOLOv11s yielding the highest mAP@0.5:0.95 under the adopted split. Because the evaluation did not include an independent test set and the bounding-box annotations were not clinically verified, these results are used only for an internal comparison of model configurations within the proof-of-concept experiment and should not be interpreted as evidence of diagnostic suitability or external generalization.

To integrate multiple neural-network and machine-learning models within a common user interface, a browser-based application architecture was adopted. The interface was implemented using React to provide platform-independent access through a standard web browser. This design facilitates access from different devices and enables the analytical modules to be integrated within a common software environment.

React was used to implement a modular web interface integrating the forecasting and image-analysis components. The application-level design is consistent with broader research on AI implementation [78], visually interactive software systems [79], platform-selection methodologies [80], deep-learning-based interactive systems [81], and intelligent decision-support architectures [82]. These studies are considered here as methodological context for software level organization rather than as direct medical analogues of the proposed system. Separate interface elements provide access to ARIMA, DNN, and LSTM forecasting outputs and to the results produced by the selected YOLO model.

The modular React-based design also simplifies system maintenance and future extension. Additional forecasting or image-analysis models can be integrated without restructuring the entire user interface, thereby improving software maintainability and scalability. The first page of the application is designed for predicting the incidence of infectious diseases (Figure 13). It allows the user to upload epidemiological data files in .csv or .xlsx format and select the type of neural network (DNN or LSTM). The user can initiate forecasting based on the uploaded data and, if necessary, perform model training. In addition, the interface provides navigation to the chest X-ray image analysis. The results of forecasting infectious diseases are shown in Figures 14–16.

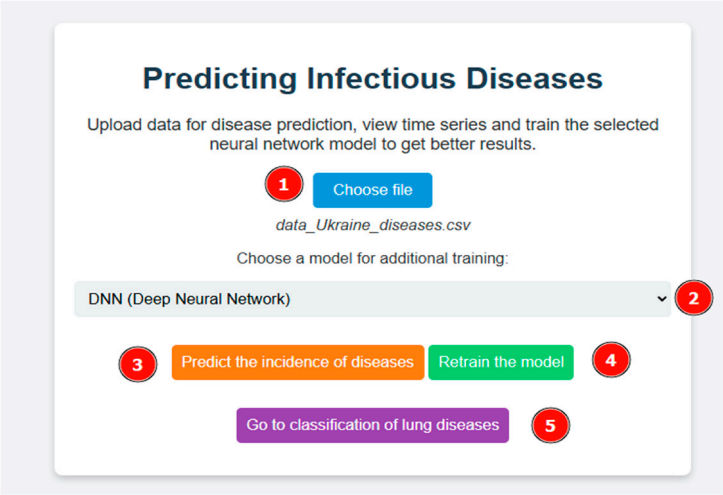


Figure 13. Web interface for infectious-disease forecasting: (1) epidemiological data file upload; (2) forecasting model selection; (3) disease incidence prediction; (4) model retraining; (5) navigation to the lung disease classification module.

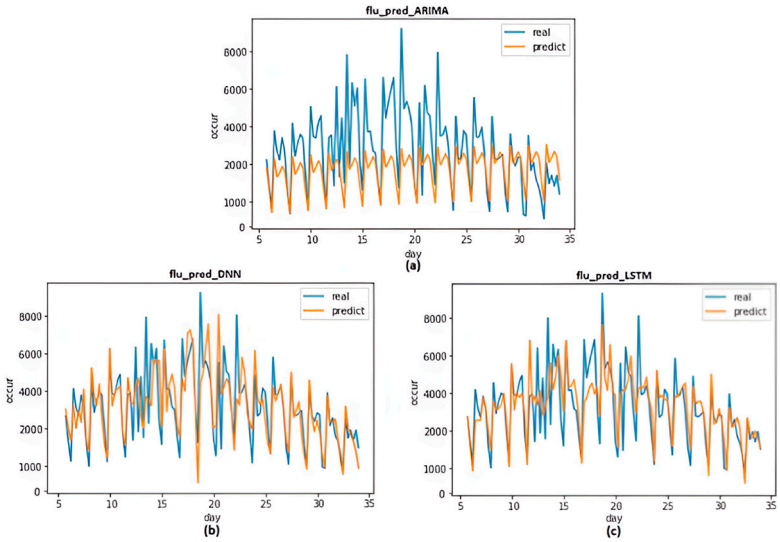


Figure 14. (**a**) Prediction graph of the ARIMA model for flu; (**b**) prediction graph of the DNN model with the best performance for flu; (**c**) prediction graph of the LSTM model with the best performance for flu.

The AIC and RMSE values obtained for the three best seasonal ARIMA configurations for each disease are presented in Table 3.

Table 3. Candidate seasonal ARIMA configurations, corresponding AIC, and RMSE values.

Disease	Models	AIC	RMSE
Measles	ARIMA(1,1,1)(1,0,0), ARIMA(2,1,2)(1,0,0), ARIMA(1,1,1)(2,0,1)	1540.740, 1540.821, 1541.651	3.278, 3.274, 3.278
ARI	ARIMA(1,0,1)(1,0,0), ARIMA(1,0,2)(1,0,0) ARIMA(1,0,1)(1,1,0)	3615.640, 3615.891, 3615.129	55.728, 56.320, 57.015
Flu	ARIMA(1,0,1)(0,1,0) ARIMA(1,0,2)(1,1,2) ARIMA(2,0,1)(1,1,1)	4665.911, 4694.192, 4701.994	100.302, 101.258, 102.456

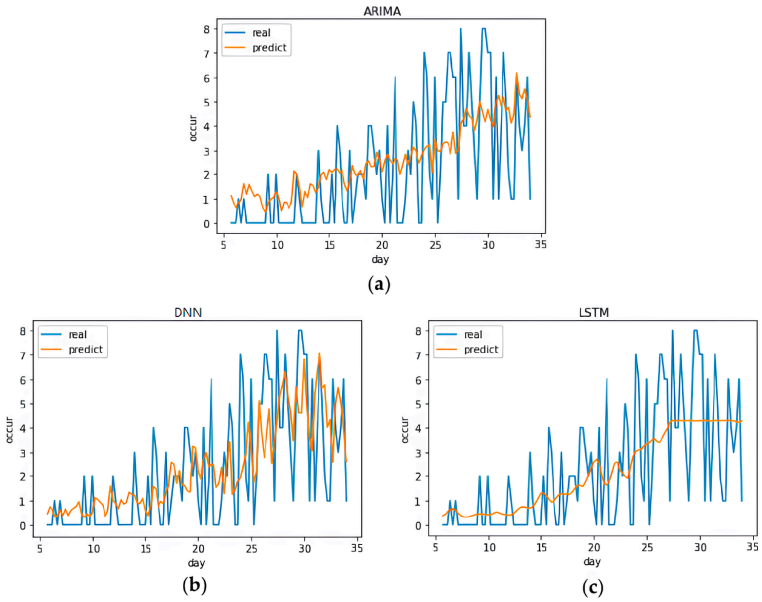


Figure 15. (**a**) Prediction graph of the ARIMA model for measles; (**b**) prediction graph of the DNN model with the best performance for measles; (**c**) prediction graph of the LSTM model with the best performance for measles.

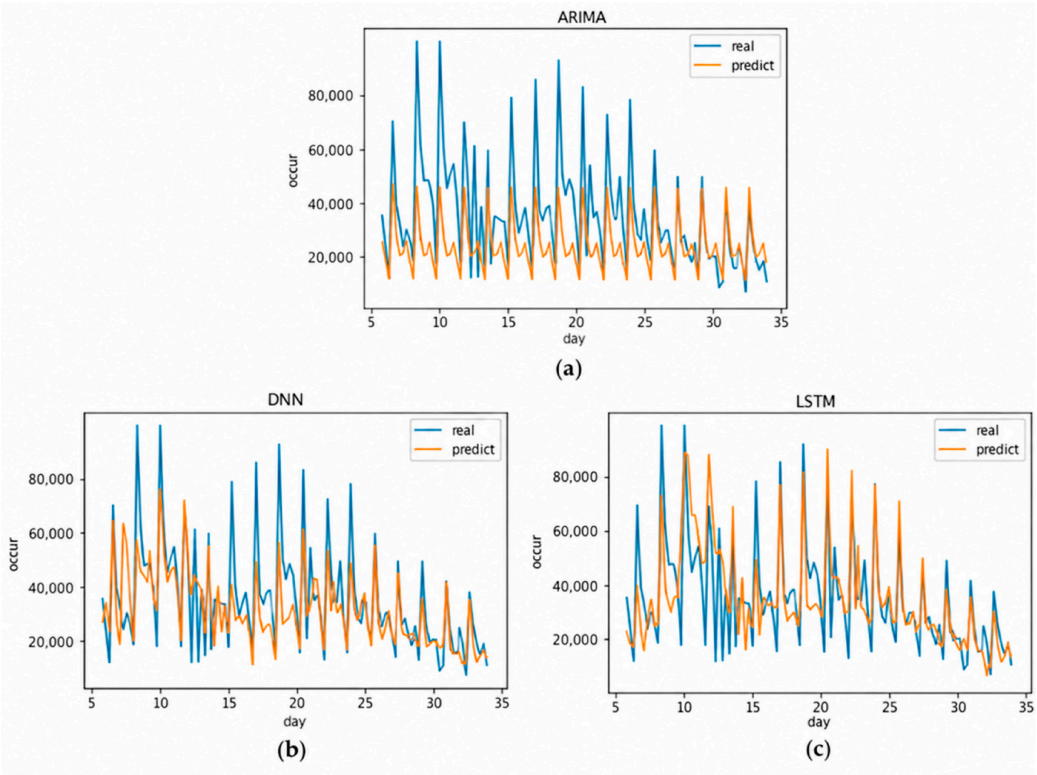


Figure 16. (**a**) Prediction graph of the ARIMA model for ARI; (**b**) prediction graph of the DNN model with the best performance for ARI; (**c**) prediction graph of the LSTM model with the best performance for ARI.

The one-month-ahead forecasting results obtained for influenza are presented in Figure 14.

The one-month-ahead forecasted incidence of measles was compared with the original dataset (Figure 15).

Similarly, the one-month-ahead forecasted incidence of ARI (Acute Respiratory Infections) was analyzed against the original data. The corresponding one-month-ahead forecasting results for ARI are presented in Figure 16.

Figure 17 shows the main page of the implemented chest X-ray image-analysis module, labeled "Lung Disease Detector" in the prototype interface. The interface allows the user to access usage instructions, upload a chest X-ray image, initiate analysis using the YOLOv11n model implemented in the prototype, and return to the forecasting module. Representative images from the validation subset were then processed through the web-based image-analysis module to demonstrate the end-to-end application workflow; the corresponding outputs are shown in Figure 18.

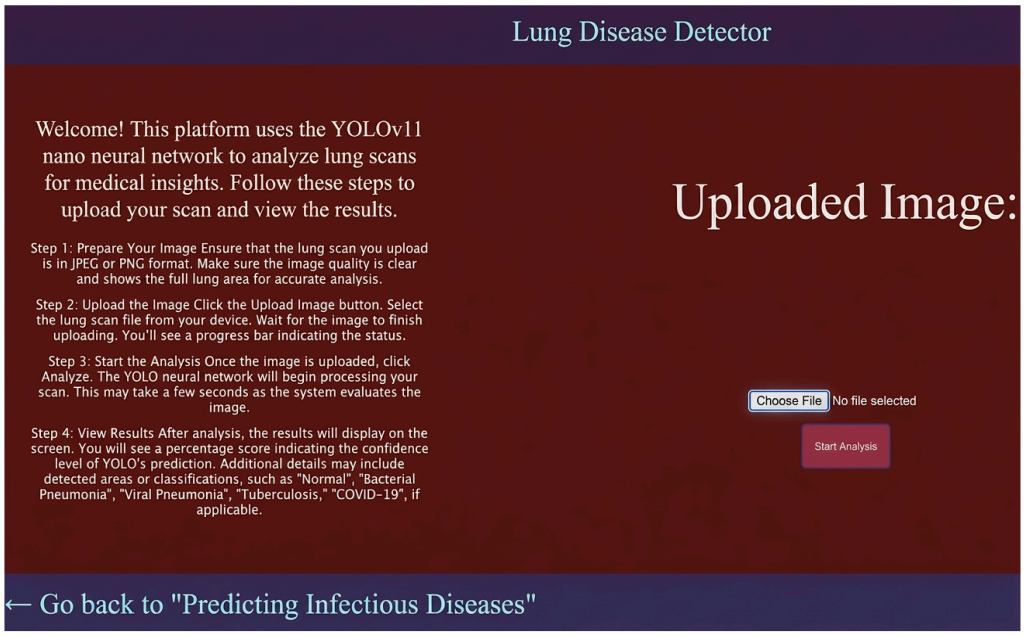


Figure 17. Main page of the "Lung Disease Detector" module.

Combining epidemiological forecasting and chest X-ray image analysis within a common application environment provides access to complementary population-level and individual-level model outputs through a single interface. The forecasting component produces one-month-ahead incidence estimates under the adopted hold-out scenario, while the YOLO-based component provides preliminary class, localization, and confidence outputs for chest X-ray images. The image-analysis module is intended solely as a proof-of-concept computational component and not as a clinically validated diagnostic or treatment-support tool.

Further experiments in training YOLO models could provide deeper insights into fine-tuning models for specific tasks, paving the way for improvements tailored to medical applications [83–85].

The common interface demonstrates the technical integration of population-level forecasting and individual-level image-analysis functions within a single application environment; the present study does not establish improved clinical or operational decision-making.

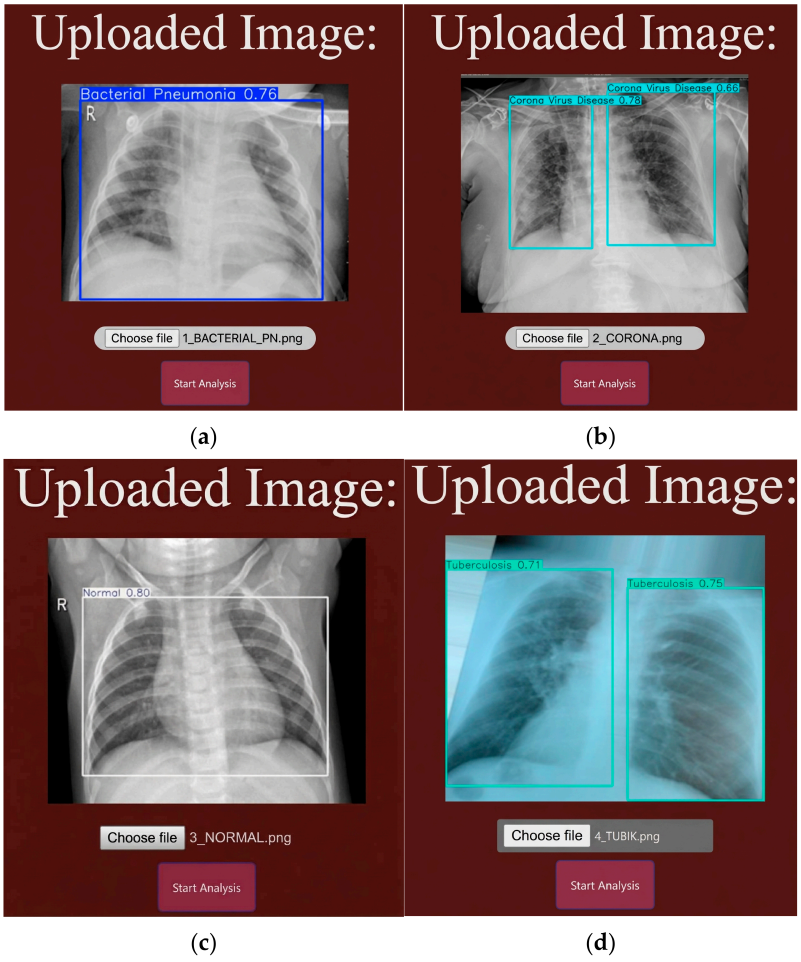


Figure 18. (**a**) Representative outputs of the web-based image-analysis module for validation-subset images labeled as: (**a**) bacterial pneumonia; (**b**) COVID-19; (**c**) normal lungs; and (**d**) tuberculosis.

5. Discussion and Conclusions

The results of this study demonstrate the technical feasibility of integrating time series forecasting and proof-of-concept chest X-ray image analysis as complementary analytical functions within a common application environment. The two modules are integrated only at the application level, while the underlying forecasting and image-analysis models remain methodologically independent. This design provides a common interface for population-level epidemiological monitoring and preliminary patient-level image analysis without implying joint learning or multimodal data fusion.

Under the adopted one-month-ahead evaluation scenario, DNN and LSTM provided better forecasting results than the classical ARIMA model for most of the considered disease series. These findings characterize the specific December 2023 hold-out experiment and should not be interpreted as evidence of a universally superior forecasting approach. One possible explanation for this behavior is the ability of neural network models to represent nonlinear temporal dependencies; however, the limited temporal validation does not allow this explanation to be confirmed conclusively. At the same time, ARIMA demonstrates stable performance for relatively stationary segments of the time series, which confirms its applicability as a baseline model. The observed results suggest a potential advantage of recurrent modeling for rapidly changing temporal patterns, although validation across multiple forecasting origins is required to confirm this tendency. The observed advantage of neural network forecasting over the classical ARIMA baseline is generally consistent with previous studies. In [11], LSTM demonstrated lower forecasting errors than ARIMA

for COVID-19 incidence and mortality data, supporting the ability of recurrent architectures to represent nonlinear temporal dependencies. Similarly, the hybrid forecasting approaches examined in [12] showed that combining statistical and neural network components may improve predictive performance compared with conventional models. The results obtained in the present study follow the same general tendency, as DNN and LSTM provide better forecasting performance than ARIMA in most of the considered cases. However, direct numerical comparison with [10–13] is not appropriate because the studies differ in terms of diseases, geographical regions, forecasting horizons, dataset sizes, and evaluation metrics. In contrast to these previous works, the present study evaluates ARIMA, DNN, and LSTM within a common application scenario using Ukrainian epidemiological data for measles, acute respiratory infections, and influenza under emergency conditions.

The forecasting evaluation is also subject to an important temporal-validation limitation. The comparative experiment uses December 2023 as a single held-out forecasting point for all three approaches. Although this provides a common one-step-ahead evaluation condition for ARIMA, DNN, and LSTM, performance at a single temporal origin is insufficient to establish the stability of the observed model ranking across different periods. The forecasting results should therefore be interpreted as a preliminary comparison under the adopted hold-out scenario. Future work should employ rolling-origin or walk-forward evaluation over multiple forecasting points and report aggregated error metrics to obtain a more robust estimate of out-of-sample forecasting performance.

Recent research on neural network forecasting of non-stationary infectious disease time series has also demonstrated that forecasting accuracy can be improved by optimizing the model input space and selecting informative exogenous variables without increasing architectural complexity. For the proposed system, this provides a concrete direction for extending the forecasting module with carefully selected calendar, demographic, mobility, and emergency-related indicators that may capture structural changes not represented by lagged incidence values alone.

In the image-analysis experiment, YOLOv11s produced the highest validation mAP@0.5:0.95 among the four evaluated configurations, reaching 0.74 under the adopted validation partition. This value should not be interpreted as an estimate of performance on independent or clinical data because the public dataset had been augmented before acquisition, no independent test subset was used, and the manually prepared bounding-box annotations were not clinically verified. The observed metric differences therefore characterize only the relative behavior of the evaluated YOLO configurations within the present proof-of-concept experiment. Although YOLOv11s produced a higher validation mAP@0.5:0.95 than the evaluated YOLOv8 variants, the current experimental design does not support conclusions regarding superior external generalization or diagnostic reliability.

The image-analysis results should also be considered in relation to previous studies. The Lung-DT framework presented in [14] demonstrated high performance using YOLOv8 for thoracic image analysis and partially relied on the same publicly available chest X-ray dataset considered in this work. Nevertheless, the numerical results are not directly comparable because [14] used a different dataset composition, experimental protocol, and primarily classification-oriented metrics, whereas the present study evaluates bounding-box-based object detection using mAP@0.5:0.95. The findings of [15] further indicate that respiratory-image classification performance depends substantially on architecture selection and training configuration, which is consistent with the differences observed between the YOLOv8 and YOLOv11 configurations in this study. Studies [16] and [17] provide additional examples of YOLO-based approaches applied to pulmonary imaging; however, they focus on different imaging modalities or disease groups and use different

experimental protocols, so their reported results are not directly comparable with those obtained in the present study.

At the system level, the contribution of the present work differs from the individual algorithmic approaches reviewed in Section 2. The forecasting and image-analysis modules remain methodologically independent and are integrated at the application level through a common web-based environment. Thus, the contribution should not be interpreted as joint learning or multimodal data fusion. Instead, the implemented prototype demonstrates the application-level integration of population-level forecasting and individual-level image-analysis functionality within a single analytical interface.

The comparison was intentionally limited to YOLOv8 and YOLOv11 nano and small configurations and should therefore not be interpreted as an exhaustive benchmark of all available YOLO generations. Evaluation of additional detector architectures represents a direction for future work.

A comparison with [14] is particularly relevant because the Lung-DT study partially relied on the same publicly available chest X-ray dataset. Lung-DT reported considerably higher classification-oriented accuracy; however, its experimental protocol differs substantially from that used in the present study. The authors combined the considered dataset with an additional chest X-ray dataset, used a different data partitioning strategy, and evaluated their model primarily using classification metrics. In contrast, the present work employs manually prepared bounding-box annotations and evaluates YOLO models using object-detection metrics, including mAP@0.5:0.95. Consequently, the reported numerical values should not be interpreted as directly comparable measures of model performance. Rather, the comparison illustrates that reported numerical results depend strongly on dataset composition, task formulation, annotation strategy, and evaluation protocol, and therefore should be interpreted within the context of the corresponding experimental design.

Qualitative inspection of the validation-subset outputs indicates that some prediction errors occur between visually similar annotated categories, including the normal-lung category and disease categories with relatively subtle image patterns. Because the annotations were not independently verified by a clinical expert, these observations should be interpreted only as descriptive characteristics of the current validation partition and not as evidence regarding clinical diagnostic behavior. Such variability further emphasizes the importance of high-quality, independently verified annotations and robust data-preparation procedures in medical-image studies. Although the cited method was developed for cardiogram parameters, the same data-quality principle is relevant to radiographic analysis, where acquisition noise, contrast variability, and source-dependent artifacts may affect model predictions. In addition, the presence of overlapping visual patterns between different disease categories may further complicate the classification process.

It is important to note that the size and composition of the dataset represent a limiting factor in this study. An additional limitation concerns the augmentation history of the public chest X-ray dataset. Because augmentation had been performed by the dataset provider before the dataset was acquired, and the correspondence between augmented samples and their original source images was not available, the available train–validation partition may have placed transformed variants of the same original image into different subsets. Therefore, the possibility of data leakage cannot be excluded, and the reported image-analysis metrics may be optimistic. They should be interpreted solely as results obtained under the current validation partition and not as estimates of performance on independent datasets or of clinical generalization.

The additional perceptual-hash audit provided a descriptive quantitative estimate of this issue. No byte-identical cross-partition files were identified, while the strict pHash

threshold of $\leq$4 yielded 54 candidate pairs involving 41 validation images (2.03% of the validation subset). However, these results do not establish source-level independence. Perceptual hashing measures visual similarity rather than image provenance; therefore, low-distance matches do not prove a common original source, while transformed variants originating from the same source may also remain undetected when stronger geometric or photometric augmentation has been applied.

Future image-analysis experiments should perform source-level or group-aware partitioning before augmentation so that all transformed variants derived from the same original image remain within a single subset. Such a procedure would provide a stronger basis for unbiased evaluation than post hoc similarity analysis of an already augmented dataset.

An appropriate external dataset for direct validation of the complete five-category detection task was not identified. Available public chest X-ray datasets differ from the dataset used in this study in terms of disease taxonomy and/or annotation format and do not simultaneously provide the five considered categories, such as bacterial pneumonia, COVID-19, tuberculosis, viral pneumonia, and normal lungs, together with directly compatible bounding-box annotations. Consequently, external evaluation using these datasets would require category remapping or modification of the task definition, and the resulting metrics would not constitute a directly comparable validation of the present five-category detection setting. Therefore, the reported image-analysis metrics are specific to the adopted validation partition and should not be interpreted as estimates of external or clinical generalization. Independent external validation using a suitably matched and clinically curated chest X-ray dataset remains necessary and is considered an important requirement for future work.

A further limitation concerns the annotation protocol. Although the bounding-box annotations required for YOLO training were manually prepared for this study, they were not independently validated by a qualified radiologist or another clinical specialist. Consequently, the resulting annotations cannot be considered clinically validated ground truth. The reported image-analysis results should therefore be interpreted as a proof-of-concept evaluation of the computational pipeline rather than as evidence of clinically validated diagnostic performance. Future studies should include expert annotation or independent review by qualified medical specialists, preferably with inter-rater agreement assessment.

Beyond the partition-related leakage risk, the public dataset may not capture the diversity of chest X-ray images encountered across institutions and acquisition conditions. Future work should therefore evaluate larger multi-source datasets and consider domain-adaptation strategies.

At the system level, the current forecasting and image analysis modules remain methodologically independent and are connected only through the common web interface. Future research may investigate whether limited information exchange between the modules can provide measurable benefits; however, such extensions would require a dedicated cross-module validation protocol and are outside the scope of the present study. In the current prototype, the web interface serves as a common access layer for the two analytical functions.

Overall, the study demonstrates that machine-learning-based time series forecasting and deep-learning-based image analysis can be implemented as complementary computational functions within a common web-based environment. The forecasting component provides population-level one-month-ahead estimates under the adopted temporal hold-out scenario, whereas the image-analysis component provides preliminary model outputs for chest X-ray images under the adopted validation partition. The present evaluation demonstrates technical integration and comparative model behavior within the available

datasets but does not establish clinical effectiveness, diagnostic reliability, or operational decision-support performance.

Despite the identified limitations, the present proof-of-concept results provide a basis for further methodological development and independent validation of the proposed system. Future improvements may include optimization of model architectures, incorporation of additional data sources, and extension of the system to other types of diseases and imaging modalities. These directions may contribute to the development of more robust and scalable intelligent systems for healthcare applications. Future work will prioritize independent external validation on clinically curated chest X-ray data with a disease taxonomy and annotation protocol compatible with the present task. Where exact category compatibility cannot be achieved, future studies should define a dedicated harmonization protocol before cross-dataset evaluation.

Overall, the study demonstrates the feasibility of exposing two complementary analytical functions through a common web-based prototype. The forecasting module provides one-month-ahead incidence estimates under the adopted hold-out scenario, while the image-analysis module provides validation-partition model outputs for chest X-rays. These findings should be interpreted as proof-of-concept computational results rather than as validation of operational or clinical effectiveness.

Author Contributions: Conceptualization, M.S. and D.C.; methodology, M.S., Y.K. and I.S.; software, M.S.; validation, Y.K., D.C. and G.K.; formal analysis, I.S. and G.K.; investigation, D.C., Y.K. and M.S.; resources, M.S., G.K. and D.C.; data curation, Y.K. and I.S.; writing—original draft preparation, M.S. and I.S.; writing—review and editing, Y.K. and D.C.; visualization, M.S. and G.K.; supervision, Y.K. and I.S.; project administration, Y.K., I.S. and D.C.; funding acquisition, D.C. All authors have read and agreed to the published version of the manuscript.

Funding: The study was funded by the National Research Foundation of Ukraine in the framework of the research project 2025.07/0270 on the topic "A Multidisciplinary Methodology for Modelling the Syndemic of War: Infectious Diseases, Information Manipulation, and Challenges of Incomplete Medical Data During Conflicts."

Data Availability Statement: Data will be made available on reasonable request.

Conflicts of Interest: The authors declare no conflicts of interest.

Abbreviations

The following abbreviations are used in this manuscript:

ARIMA	Autoregressive Integrated Moving Average
DNN	Deep Neural Network
LSTM	Long Short-Term Memory
YOLO	You Only Look Once
CNN	Convolutional Neural Network
MSE	Mean Squared Error
RMSE	Root Mean Squared Error
MAE	Mean Absolute Error
MAPE	Mean Absolute Percentage Error
AIC	Akaike Information Criterion
mAP	Mean Average Precision
IoU	Intersection over Union
NLP	Natural Language Processing
BPNN	Backpropagation Neural Network

References

1. Morens, D.M.; Fauci, A.S. Emerging Pandemic Diseases: How We Got to COVID-19. *Cell* **2020**, *182*, 1077–1092. [CrossRef] [PubMed]
2. Alotaibi, A.M. Explainable Long-Sequence Time-Series Forecasting for Infectious Diseases Using Optimised Transformer Models. *Int. J. Data Sci. Anal.* **2026**, *21*, 8. [CrossRef]
3. Pylypenko, O.; Kivva, S.; Brovchenko, I. Modelling System for Decision Support of Epidemic Diseases in Ukraine. In *Mathematical Modeling and Simulation of Systems*; MODS 2024; Kazymyr, V., Morozov, A., Palagin, A., Shkarlet, S., Stoianov, M., Vinnikov, D., Zheleznyak, M., Eds.; Lecture Notes in Networks and Systems; Springer: Cham, Switzerland, 2025; Volume 1391, pp. 68–80. [CrossRef]
4. Chumachenko, D.; Chumachenko, T. Impact of War on the Dynamics of COVID-19 in Ukraine. *BMJ Glob. Health* **2022**, *7*, e009173. [CrossRef] [PubMed]
5. Yutilova, K.; Shved, E.; Rozantsev, G.; Adamski, A. Russia–Ukraine War Impacts on Environment: Warfare Chemical Pollution and Recovery Prospects. *Environ. Sci. Pollut. Res.* **2025**, *32*, 5685–5702. [CrossRef] [PubMed]
6. Chumachenko, D.; Bazilevych, K.; Butkevych, M.; Meniailov, I.; Parfeniuk, Y.; Sidenko, I.; Chumachenko, T. Methodology for Assessing the Impact of Emergencies on the Spread of Infectious Diseases. *Radioelectron. Comput. Syst.* **2024**, *3*, 6–26. [CrossRef]
7. Kovaliv, O.; Kondratenko, Y.; Sidenko, I.; Kondratenko, G.; Chumachenko, D. the Accuracy of Infectious Disease Forecasts Based on Comparing Neural Network Architectures. *Computation* **2026**, *14*, 54. [CrossRef]
8. Kannan, A.; Chen, R.; Akhtar, Z. Use of Open-Source Epidemic Intelligence for Infectious Disease Outbreaks, Ukraine 2022. *Emerg. Infect. Dis.* **2024**, *30*, 9. [CrossRef] [PubMed]
9. Sheremet, A.; Kondratenko, Y.; Sidenko, I.; Kondratenko, G. Diagnosis of Lung Disease Based on Medical Images Using Artificial Neural Networks. In Proceedings of the 3rd Ukraine Conference on Electrical and Computer Engineering (UKRCON), Lviv, Ukraine, 26–28 August 2021; pp. 561–565. [CrossRef]
10. Singh, S.; Mittal, S.; Singh, S. Analysis and Forecasting of COVID-19 Pandemic Using ARIMA Model. *IEEE Access* **2023**, *11*, 143–148. [CrossRef]
11. Pane, S.F.; Adiwijaya; Sulistiyo, M.D. LSTM and ARIMA for Forecasting COVID-19 Positive and Mortality Cases in DKI Jakarta and West Java. In Proceedings of the International Conference on Informatics, Computing and Applied Mathematics (ICIC), Bali, Indonesia, 8–9 December 2022. [CrossRef]
12. Jin, Y.-C.; Cao, Q.; Wang, K.-N. Prediction of COVID-19 Data Using Improved ARIMA-LSTM Hybrid Forecast Models. *IEEE Access* **2023**, *11*, 67956–67967. [CrossRef]
13. Sharma, S.; Sharma, V.K.; Aggarwal, R. Covid-19 Pandemic Predictive System Using Machine Learning. In Proceedings of the International Conference on Advances in Computing, Communication & Networking (ICAC3N), Great Noida, India, 16–17 December 2022. [CrossRef]
14. Avanzato, R.; Beritelli, F. Lung-DT: An AI-Powered Digital Twin Framework for Thoracic Health Monitoring and Diagnosis. *Sensors* **2024**, *24*, 958. [CrossRef] [PubMed]
15. Atamanyuk, I.; Kondratenko, Y.; Trofymenko, Y.; Sidenko, I.; Chumachenko, D.; Poltorak, A. The Features of Using Neural Networks for Classification of Respiratory Diseases on X-Ray Images. In Proceedings of the 24th International Industrial Simulation Conference (ISC 2026), San Sebastian, Spain, 27–29 May 2026; ISBN 978-9-492859-40-2.
16. Wang, L.; Zhang, C.; Zhang, Y. An Automated Diagnosis Method for Lung Cancer Target Detection and Subtype Classification Based on CT Scans. *Bioengineering* **2024**, *11*, 767. [CrossRef] [PubMed]
17. Mousavi, M.; Mirshafiee, F.S.; Shahbazi, E. YOLO for Lung Disease Detection from CT Scans. In Proceedings of the IEEE International Symposium on Intelligent Systems and Informatics (SISY), Pula, Croatia, 21–23 September 2023. [CrossRef]
18. Sharma, A.; Kumar, V.; Longchamps, L. Comparative Performance of YOLOv8, YOLOv9, YOLOv10, YOLOv11 and Faster R-CNN Models for Detection of Multiple Weed Species. *Smart Agric. Technol.* **2024**, *9*, 100648. [CrossRef]
19. Xu, D.; Chan, W.H.; Haron, H.; Nies, H.W.; Moorthy, K. From COVID-19 to Monkeypox: A Novel Predictive Model for Emerging Infectious Diseases. *BioData Min.* **2024**, *17*, 42. [CrossRef] [PubMed]
20. Cheng, C.; Aruchunan, E.; Noor Aziz, M.H. Leveraging Dynamics Informed Neural Networks for Predictive Modeling of COVID-19 Spread: A Hybrid SEIRV-DNNs Approach. *Sci. Rep.* **2025**, *15*, 2043. [CrossRef] [PubMed]
21. Filist, S.; Al-Kasasbeh, R.T.; Gevorkyan, T.G.; Habahbeh, O.M.A.; Shatalova, O.; Telfah, A.; Starkov, E.; Korenevskiy, N.A.; Shaqadan, A.; Namazov, M.B.; et al. Advanced Bioimpedance Analysis for Infectious Disease Risk Assessment via Neural Network Classifiers. *Phys. Eng. Sci. Med.* **2025**, *48*, 1167–1183. [CrossRef] [PubMed]
22. Ahmad, M.J.; Günel, K. Can Neural Networks Estimate Parameters in Epidemiology Models Using Real Observed Data? *Appl. Intell.* **2025**, *55*, 133. [CrossRef]
23. Kondratenko, Y.; Sichevskyi, S.; Kondratenko, G.; Sidenko, I. Manipulator's Control System with Application of the Machine Learning. In Proceedings of the 11th IEEE International Conference on Intelligent Data Acquisition and Advanced Computing Systems: Technology and Applications (IDAACS), Cracow, Poland, 22–25 September 2021. [CrossRef]

24. Kondratenko, G.; Sidenko, I.; Saliutin, M.; Kondratenko, Y. Mobile Recognition of Image Components Based on Machine Learning Methods. *J. Mob. Multimed.* **2024**, *20*, 699–726. [CrossRef]
25. Sova, I.; Sidenko, I.; Kondratenko, Y. Machine Learning Technology for Neoplasm Segmentation on Brain MRI Scans. In *CEUR Workshop Proceedings*; CEUR-WS: Aachen, Germany, 2020; Volume 2791, pp. 50–59. Available online: https://ceur-ws.org/Vol-2791/2020200050.pdf (accessed on 14 October 2026).
26. Yu, Q.; Yang, G.; Wang, X.; Shi, Y.; Feng, Y.; Liu, A. A Review of Time Series Forecasting and Spatio-Temporal Series Forecasting in Deep Learning. *J. Supercomput* **2025**, *81*, 1160. [CrossRef]
27. Bakouch, H.S.; Gabr, M.M.; El-Desouky, B.S.; El-Hadidy, S.M. On Shifted INAR(1) Time Series with Intervened Geometric Innovations: Properties, Forecasting with Modeling Crime and Industry Data. *Iran. J. Sci.* **2026**, *50*, 293–314. [CrossRef]
28. Song, Z.; Lu, Q.; Xu, H.; Yang, Z.; Zhu, H.; Buckeridge, D.; Li, Y. Timelygpt: Extrapolatable Transformer Pre-Training for Long-Term Time-Series Forecasting in Healthcare. *Health Inf. Sci. Syst.* **2025**, *13*, 64. [CrossRef] [PubMed]
29. Ghosh, S.K.; Ananthakumar, U.; Chougale, P.D.; Somaraj, A.B. Forecasting Malaria in Indian States: A Time Series Approach with R Shiny Integration. *Malar. J.* **2025**, *24*, 403. [CrossRef] [PubMed]
30. Chukwu, C.W. Forecasting and Quantifying the Role of Vaccination Strategies in the 2025 Texas Measles Outbreak: A Modeling and Time Series Analysis Approach. *BMC Infect. Dis.* **2026**, *26*, 530. [CrossRef] [PubMed]
31. Li, Y.H.; Qin, Y.S. Empirical Likelihood for Autoregressive Models with Spatial Errors. *Acta Math. Appl. Sin. Engl. Ser.* **2025**, *41*, 775–796. [CrossRef]
32. Balzer, M. Fast and Scalable Variable Selection for Spatial Autoregressive Models: M. Balzer. *Stat. Pap.* **2026**, *67*, 38. [CrossRef]
33. Sokoliuk, A.; Kondratenko, G.; Sidenko, I.; Kondratenko, Y.; Khomchenko, A.; Atamanyuk, I. Machine Learning Algorithms for Binary Classification of Liver Disease. In Proceedings of the 2020 IEEE International Conference on Problems of Infocommunications Science and Technology (PIC S&T), Kharkiv, Ukraine, 6–9 October 2020. [CrossRef]
34. Cheng, Y.; Bai, Y.; Yang, J.; Tan, X.; Xu, T.; Cheng, R. Analysis and Prediction of Infectious Diseases Based on Spatial Visualization and Machine Learning. *Sci. Rep.* **2024**, *14*, 28659. [CrossRef] [PubMed]
35. Xu, S.; Chen, L.; Luo, J.; Hu, B. Trends in Epidemics Pertaining to Notifiable Infectious Diseases in China and Prediction Models for Key Diseases: A Case Study of Ziyang County. *BMC Public Health* **2025**, *25*, 4099. [CrossRef] [PubMed]
36. Zheng, X.; Qiao, L.; Hong, H.; Zhang, Y.; Fan, Q.; Dai, J.; Zhao, J.; Yao, F.; Shen, S. Predicting the Incidence of Common Intestinal Infectious Diseases in Changzhou, China Based on Environmental Factors and Deep Learning. *BMC Public Health* **2026**, *26*, 319. [CrossRef] [PubMed]
37. Yu, J.; Wang, H.; Chen, M.; Han, X.; Deng, Q.; Yang, C.; Zhu, W.; Ma, Y.; Yin, F.; Weng, Y.; et al. A Novel Method to Select Time-Varying Multivariate Time Series Models for the Surveillance of Infectious Diseases. *BMC Infect. Dis.* **2024**, *24*, 832. [CrossRef] [PubMed]
38. Liu, J.; Zhang, Z.; Lyu, B.; Feng, R.; He, Y. A Hybrid ARIMA-BP Approach for Superior Accuracy in Predicting Traffic Accident Losses. *Sci. Rep.* **2025**, *15*, 24328. [CrossRef] [PubMed]
39. Chumnaul, J.; Damkliang, K. Integrating Quantile Regression with ARIMA and ANN for Interpretable and Accurate PM2.5 Forecasting in Hat Yai, Thailand. *Sci. Rep.* **2025**, *15*, 43352. [CrossRef] [PubMed]
40. Zhou, Q.; Hu, J.; Hu, W.; Li, H.; Lin, G.-Z. Interrupted Time Series Analysis Using the ARIMA Model of the Impact of COVID-19 on the Incidence Rate of Notifiable Communicable Diseases in China. *BMC Infect. Dis.* **2023**, *23*, 375. [CrossRef] [PubMed]
41. Saikia, J.; Goswami, K.; Kakaty, S.C. Wavelet-SARIMA-Transformer: A Hybrid Model for Rainfall Forecasting. *Theor. Appl. Climatol.* **2026**, *157*, 109. [CrossRef]
42. Mondal, S.K.; Ahmmad, S.; Khan, S.; Chowdhury, M.H.; Paul, G.K.; Binyamin; Gupta, P.S.; Purohit, S.; Chakrabortty, R. Modeling and Forecasting Monthly Humidity in South Asia: A SARIMA Approach. *Earth Syst. Environ.* **2026**, *10*, 493–509. [CrossRef]
43. Soltani, K.; Azari, A.; Zeynoddin, M.; Amiri, A.; Ebtehaj, I.; Ouarda, T.B.M.J.; Gharabaghi, B.; Bonakdari, H. Lake Surface Area Forecasting Using Integrated Satellite-SARIMA-Long-Short-Term Memory. *Model. Soft Comput.* **2026**, *30*, 3143–3165. [CrossRef]
44. Yang, W.; Ding, L.; Su, A. Comparison of SES Method and SARIMA Model in Predicting the Number of Admissions in the Department of Neurology. *Sci. Rep.* **2025**, *15*, 18287. [CrossRef] [PubMed]
45. Bartholomew, D.C.; Iwu, H.C.; Ibemere, I.P. A Hybrid Model of Artificial Neural Network and SARIMA Models for Predicting Inflation Rate Change in Nigeria's Economy. *Ann. Data Sci.* **2025**. [CrossRef]
46. Yildirim, A.; Bilgili, M. Global Monthly CO_2 Concentration Forecasting Using SARIMA and LSTM Models. *Meteorol. Atmos. Phys.* **2026**, *138*, 20. [CrossRef]
47. Xu, Q.; Li, R.; Liu, Y.; Luo, C.; Xu, A.; Xue, F.; Xu, Q.; Li, X. Forecasting the Incidence of Mumps in Zibo City Based on a SARIMA Model. *Int. J. Environ. Res. Public Health* **2017**, *14*, 925. [CrossRef] [PubMed]
48. Koohfar, S.; Woldemariam, W.; Kumar, A. Prediction of Electric Vehicles Charging Demand: A Transformer-Based Deep Learning Approach. *Sustainability* **2023**, *15*, 2105. [CrossRef]
49. Peychinov, T.; Karaivanova, A.; Mecheva, T. Predicting Traffic Load Data: ARIMA and SARIMA Comparison. *Eng. Proc.* **2025**, *100*, 29. [CrossRef]

50. Ningombam, R.; Singh, C.; Sreekumar, S.; Bhakar, R.; Padmanaban, S. Box–Cox Integrated SARIMA Model for Day-Ahead Inertia Forecasting. *Electr. Eng.* **2025**, *107*, 9135–9153. [CrossRef]
51. Lu, J.; Mo, Y.; Xiao, Z.; Xu, L.; Yao, Q. Distribution Estimation for Time Series via DNN-Based GANs with an Application to Change-Point Estimation. *Mach. Learn.* **2025**, *114*, 208. [CrossRef]
52. Li, T.; Chen, L.; Sun, H.; Hou, M.; Lei, Y.; Zhi, K. Exploring Diversity and Time-Aware Recommendations: An LSTM-DNN Model with Novel Bidirectional Dynamic Time Warping Algorithm. *Soft Comput.* **2025**, *29*, 2003–2013. [CrossRef]
53. Itzhak, N.; Tal, S.; Cohen, H.; Daniel, O.; Kopylov, R.; Moskovitch, R. Improving DNNs for Time-Series Classification Using State and Gradient Abstraction-Based Preprocessing. *Neural Comput. Appl.* **2025**, *37*, 24025–24049. [CrossRef]
54. Zhang, L. Channel Equalization in Ultraviolet Communication Based on LSTM-DNN Hybrid Model. *Sci. Rep.* **2025**, *15*, 17226. [CrossRef] [PubMed]
55. Alsaidi, S.A.A.A.; Mohammed, H.J.; Al Ogaili, R.R.N.; Dashoor, Z.A.; Alsaeedi, A.H.; Al-Shammary, D.; Ibaida, A. HawkPhish-DNN Cybersecurity Model: Adaptive Hybrid Optimization and Deep Learning for Enhanced Multi-Objective Phishing URL Detection. *Int. J. Inf. Tecnol.* **2025**, *17*, 3859–3875. [CrossRef]
56. Avazov, K.; Sevinov, J.; Temerbekova, B.; Bekimbetova, G.; Mamanazarov, U.; Abdusalomov, A.; Cho, Y.I. Hybrid Cloud-Based Information and Control System Using LSTM-DNN Neural Networks for Optimization of Metallurgical Production. *Processes* **2025**, *13*, 2237. [CrossRef]
57. Umar, H.G.A.; Yasmeen, I.; Aoun, M.; Mazhar, T.; Khan, M.A.; Jaghdam, I.H.; Hamam, H. Energy-Efficient Deep Learning-Based Intrusion Detection System for Edge Computing: A Novel DNN-KDQ Model. *J. Cloud Comput.* **2025**, *14*, 32. [CrossRef]
58. Fkirin, A.; Moursi, A.S.; Attiya, G.; El-Sayed, A.; Shouman, M.A. Hybrid Two-Level Protection System for Preserving Pre-Trained DNN Models Ownership. *Neural Comput. Appl.* **2024**, *36*, 21415–21449. [CrossRef]
59. Bhardwaj, S.; Saha, R. A Secure and Scalable Traffic Management Framework Using Hybrid DNN-CNN and Geographic Routing in V2X Networks. *Peer Peer Netw. Appl.* **2026**, *19*, 48. [CrossRef]
60. Senthil, R.; Khatwal, R. An Effective Disease Detection Analysis on Rice Leaves Using Hybrid MCSVM-DNN Predictor Architecture. *Remote Sens. Earth Syst. Sci.* **2025**, *8*, 84–97. [CrossRef]
61. Singh, U.; Saurabh, K.; Trehan, N.; Vyas, R.; Vyas, O.P. GA-LSTM: Performance Optimization of LSTM Driven Time Series Forecasting. *Comput. Econ.* **2025**, *66*, 2873–2908. [CrossRef]
62. Yu, X.; Lin, Z.; Zhou, C.; Wang, H.; Wang, M. Federated Deep Convolutional Neural Network Architecture for Renal Cancer Classification. *Discov. Comput.* **2025**, *28*, 315. [CrossRef]
63. Xie, J.; Qin, J.; Qin, X.; Li, Q.; Cui, D.; Sun, D. ECLNet: Enhancing the CNN-LSTM Networks for Multivariate Long-Term Time Series Forecasting. *Appl. Intell.* **2025**, *55*, 743. [CrossRef]
64. Yang, Y.; Zhao, C.; Huang, Y. Adaptive Hierarchical Feature Fusion and Hadamard Product LSTM for Multivariate Time Series Forecasting. *J. Supercomput.* **2025**, *81*, 1436. [CrossRef]
65. Kilinc, H.C.; Apak, S.; Ozkan, F.; Yurtsever, A. AH-GCAN-LSTM: Adaptive Hybrid-Graph Convolution Attention Network with LSTM and Genetic Optimization for Hydrological Time Series Forecasting. *Water Resour. Manag.* **2025**, *39*, 8293–8312. [CrossRef]
66. Liu, J.; Wu, Y. A Hybrid Time Series Forecasting CGAN Model Based on LSTM and Conv1D and Its Application for Load Forecasting. *Electr. Eng.* **2025**, *107*, 14881–14898. [CrossRef]
67. Ding, S.; Liu, L.; Zhang, S.; Li, M. An LSTM-Driven Thermoelectric Coupling Response Prediction Method for Shape Memory Alloy Actuators. *Sci. Rep.* **2025**, *15*, 17642. [CrossRef] [PubMed]
68. Dong, J.; Fan, J.; Zhang, J.; Liu, C.; Cheng, W. TA-LSTM: Temporal Attention LSTM for Spatiotemporal Weather Prediction. *Multimed. Syst.* **2025**, *31*, 466. [CrossRef]
69. Praveenkumar, A.; Jha, G.K.; Madival, S.D.; Lama, A.; Kumar, R.R. Deep Learning Approaches for Potato Price Forecasting: Comparative Analysis of LSTM, Bi-LSTM, and AM-LSTM Models. *Potato Res.* **2025**, *68*, 1941–1963. [CrossRef]
70. Elnady, M.; Abdelmunim, H.E. A Novel YOLO LSTM Approach for Enhanced Human Action Recognition in Video Sequences. *Sci. Rep.* **2025**, *15*, 17036. [CrossRef] [PubMed]
71. Mbatha, N.; Bencherif, H. Time Series Analysis and Forecasting Using a Novel Hybrid LSTM Data-Driven Model Based on Empirical Wavelet Transform Applied to Total Column of Ozone at Buenos Aires, Argentina (1966–2017). *Atmosphere* **2020**, *11*, 457. [CrossRef]
72. Center for Public Health of the Ministry of Health of Ukraine. Infectious Diseases of the Population of Ukraine. Available online: https://phc.org.ua/kontrol-zakhvoryuvan/inshi-infekciyni-zakhvoryuvannya/infekciyna-zakhvoryuvanist-naselennya-ukraini (accessed on 26 March 2026).
73. Rasheed, A.F.; Zarkoosh, M. YOLOv11 Optimization for Efficient Resource Utilization. *J. Supercomput.* **2025**, *81*, 1085. [CrossRef]
74. Li, Y.; Zheng, Q.; Xu, S.; Wang, P.; Wang, Y.; Song, Z.; Guo, M. YOLO-EDGE: An Object Detection Algorithm for Traffic Scenarios. *J. Supercomput.* **2025**, *81*, 840. [CrossRef]
75. Zhu, X.Y.; Hu, L.L.; Gong, L.H. Visually Secure Medical Image Encryption Algorithm Based on Improved YOLOv11 and Replacement Strategy for Region of Interest. *Nonlinear Dyn.* **2026**, *114*, 103. [CrossRef]

76. Rasheed, A.F.; Zarkoosh, M. Optimized YOLOv8 for Multi-Scale Object Detection. *J. Real-Time Image Process.* **2025**, *22*, 6. [CrossRef]
77. Dalvi, O.M. Lungs Disease Dataset (4 Types). Available online: https://www.kaggle.com/datasets/omkarmanohardalvi/lungs-disease-dataset-4-types (accessed on 26 March 2026).
78. Kondratenko, Y.; Shevchenko, A.; Zhukov, Y.; Kondratenko, G.; Striuk, O. Tendencies and Challenges of Artificial Intelligence Development and Implementation. In Proceedings of the IEEE 12th International Conference on Intelligent Data Acquisition and Advanced Computing Systems: Technology and Applications (IDAACS), Dortmund, Germany, 7–9 September 2023; pp. 221–226. [CrossRef]
79. Akhundov, V.; Kondratenko, G.; Sidenko, I.; Kondratenko, Y. Visually-Interactive Systems: Structural Optimization of Software Development. In Proceedings of the 2020 IEEE International Conference on Problems of Infocommunications Science and Technology (PIC S&T), Kharkiv, Ukraine, 6–9 October 2020. [CrossRef]
80. Kondratenko, Y.; Kondratenko, G.; Sidenko, I. Multi-Criteria Decision Making and Soft Computing for the Selection of Specialized IoT Platform. In *Advances in Intelligent Systems and Computing*; Springer: Cham, Switzerland, 5 August 2018. [CrossRef]
81. Kushneryk, P.; Kondratenko, Y.; Sidenko, I. Intelligent Dialogue System Based on Deep Learning Technology. In *CEUR Workshop Proceedings*; CEUR-WS: Aachen, Germany, 2019; Volume 2403, pp. 53–62. Available online: https://icteri.org/icteri-2020/PhDS/11110053.pdf (accessed on 14 October 2026).
82. Kondratenko, G.; Kondratenko, Y.; Sidenko, I. Fuzzy Decision Making System for Model-Oriented Academia/Industry Cooperation: University Preferences. In Proceedings of the Advances in Intelligent Systems and Computing, Cham, Switzerland, 1 November 2017. [CrossRef]
83. Kovaliv, O.; Sidenko, I.; Zhukov, Y.; Kondratenko, Y. Input Space Optimization for Neural Network–based Forecasting of Non-stationary Time Series. In *CEUR Workshop Proceedings*; CEUR-WS: Aachen, Germany, 2026; Volume 4220, pp. 189–200. Available online: https://ceur-ws.org/Vol-4220/paper15.pdf (accessed on 14 October 2026).
84. Atamanyuk, I.; Atamanyuk, I.; Kondratenko, Y.; Shebanina, E.; Dudziński, M.; Borchyk, Y.; Sadovoi, A. Computational method for diagnosing cardiovascular diseases with preliminary filtering of measurement errors of cardiogram parameters. Computational Method for Diagnosing Cardiovascular Diseases with Preliminary Filtering of Measurement Errors of Cardiogram Parameters. In Proceedings of the European Simulation and Modelling Conference (ESM 2023), Toulouse, France, 24–26 October 2023.
85. Kozlov, O.; Kondratenko, Y.; Skakodub, O. Comparative Analysis of Parametric Optimization Techniques: Fuzzy DSS for Medical Diagnostics. In *Recent Developments and the New Directions of Research, Foundations, and Applications*; Shahbazova, S.N., Abbasov, A.M., Kreinovich, V., Kacprzyk, J., Batyrshin, I.Z., Eds.; Studies in Fuzziness and Soft Computing; Springer: Cham, Switzerland, 2023; Volume 423, pp. 193–201. [CrossRef]

Disclaimer/Publisher's Note: The statements, opinions and data contained in all publications are solely those of the individual author(s) and contributor(s) and not of MDPI and/or the editor(s). MDPI and/or the editor(s) disclaim responsibility for any injury to people or property resulting from any ideas, methods, instructions or products referred to in the content.